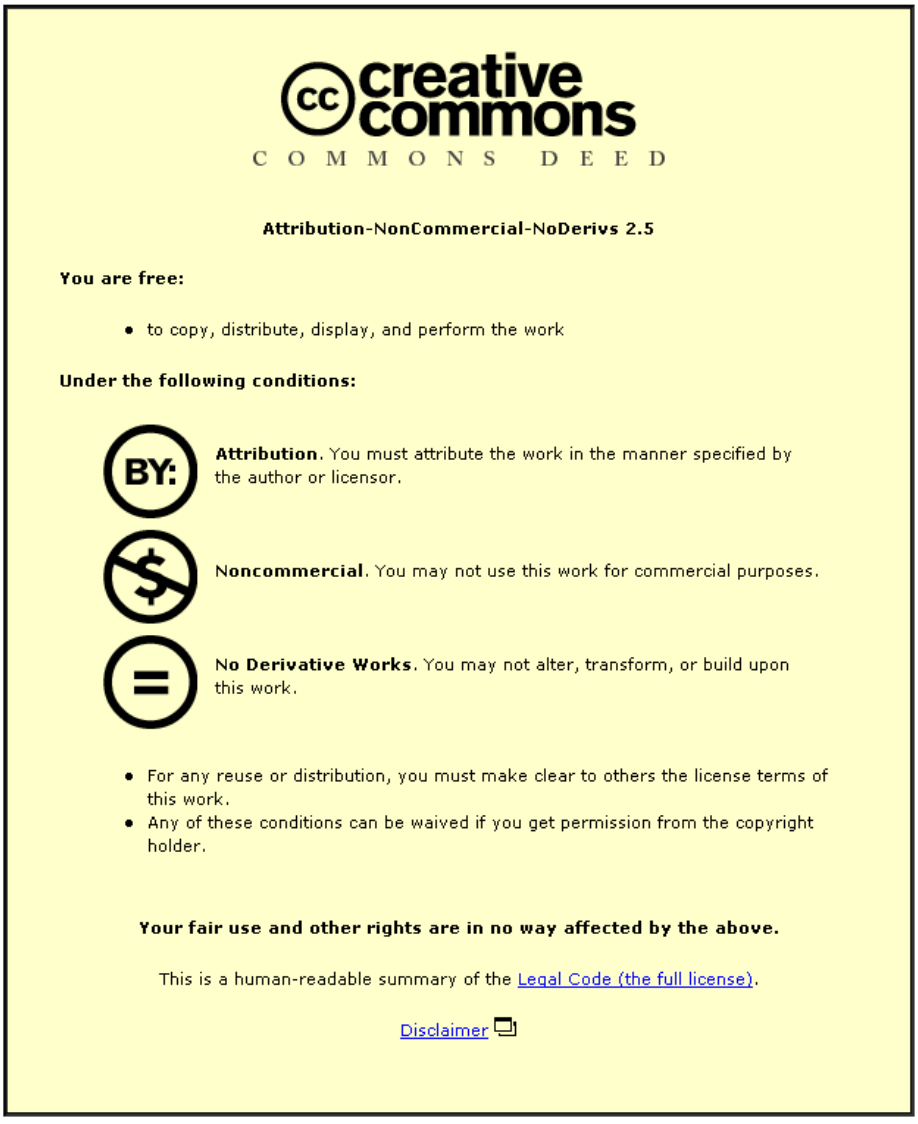

creative commons

COMMONS DEED

Attribution-NonCommercial-NoDerivs 2.5

You are free:

- to copy, distribute, display, and perform the work

Under the following conditions:

Attribution. You must attribute the work in the manner specified by the author or licensor.

Noncommercial. You may not use this work for commercial purposes.

No Derivative Works. You may not alter, transform, or build upon this work.

- For any reuse or distribution, you must make clear to others the license terms of this work.
- Any of these conditions can be waived if you get permission from the copyright holder.

Your fair use and other rights are in no way affected by the above.

This is a human-readable summary of the Legal Code (the full license).

Disclaimer

Editorial Manager(tm) for Experimental Mechanics
Manuscript Draft

Manuscript Number:

Title: Depth-resolved imaging and displacement measurement techniques viewed as linear filtering operations

Article Type: Sp Iss: Adv Image Meth

Keywords: speckle interferometry; optical coherence tomography; wavelength scanning; displacement measurement; linear filtering.

Corresponding Author: Dr. Pablo D. Ruiz, PhD

Corresponding Author's Institution: Loughborough University

First Author: Pablo D Ruiz, PhD

Order of Authors: Pablo D Ruiz, PhD; Jonathan M Huntley, Prof., PhD; Jeremy M Coupland, Prof., PhD

Abstract: The last five years have seen the emergence of a family of optical interferometric techniques that provide deformation measurements throughout three-dimensional (3-D) weakly scattering materials. They include wavelength scanning interferometry (WSI), tilt scanning interferometry (TSI), phase contrast spectral optical coherence tomography (PC SOCT) and hyperspectral interferometry (HSI) and can be thought of as a marriage between the phase sensing capabilities of Phase Shifting Interferometry and the depth-sensing capabilities of Optical Coherence Tomography. It was recently shown that some closely related 3-D optical imaging techniques can be treated as shift-invariant linear filtering operations. In this paper, we extend that work to include WSI, TSI, PC SOCT and HSI as spatial filtering operations and also relate the properties of their transfer functions in the spatial frequency domain to their spatial resolution and phase sensitivity, for depth-resolved displacement measurements.

Depth-resolved imaging and displacement measurement techniques viewed as linear filtering operations

P. D. Ruiz, J. M. Huntley and J. M. Coupland

Loughborough University

Wolfson School of Mechanical and Manufacturing Engineering

Loughborough LE11 3TU, United Kingdom

e-mail: p.d.ruiz@lboro.ac.uk

tel:+44 1509 227660; fax: +44 1509 227648

Abstract. The last five years have seen the emergence of a family of optical interferometric techniques that provide deformation measurements throughout three-dimensional (3-D) weakly scattering materials. They include wavelength scanning interferometry (WSI), tilt scanning interferometry (TSI), phase contrast spectral optical coherence tomography (PC SOCT) and hyperspectral interferometry (HSI) and can be thought of as a marriage between the phase sensing capabilities of Phase Shifting Interferometry and the depth-sensing capabilities of Optical Coherence Tomography. It was recently shown that some closely related 3-D optical imaging techniques can be treated as shift-invariant linear filtering operations. In this paper, we extend that work to include WSI, TSI, PC SOCT and HSI as spatial filtering operations and also relate the properties of their transfer functions in the spatial

frequency domain to their spatial resolution and phase sensitivity, for depth-resolved displacement measurements.

Keywords: Phase imaging, speckle interferometry, optical coherence tomography, wavelength scanning, frequency scanning, tilt scanning, displacement measurement, linear filtering.

1. Introduction

The use of phase information to provide data on displacement, strain and velocity fields has become widespread in experimental solid and fluid mechanics. In solid mechanics, optical techniques such as speckle and moiré interferometry, or digital holography, provide phase images related to the deformation state of the surface of a 3-D object. In fluid mechanics, holographic particle image velocimetry and Doppler OCT can be used to measure internal velocity fields. Increasing the dimensionality of the measurements, whether through the addition of a further spatial axis, time axis, or wavenumber axis, provides information that can increase the reliability of both the process of phase unwrapping, and of subsequent application specific post-processing steps such as estimation of the elastic modulus fields. From an experimental viewpoint, the simplest approach to increasing the dimensionality of the measurement is through the addition of a time axis. Providing the frequency of the interference signal lies below the temporal Nyquist limit for the camera being used, the phase can be tracked as a function of time at each camera pixel. An alternative to the ‘2 spatial + time’ axes, involves the acquisition of time independent data that allows phase volumes to be reconstructed along all three spatial coordinates.

Wavelength scanning interferometry [1, 2], tilt scanning interferometry [3, 4], phase contrast spectral optical coherence tomography [5, 6] and hyperspectral interferometry [7] have been developed over the past five years and can be regarded as a combination of the depth-sensing capabilities of optical coherence tomography and the phase-sensitive capabilities of traditional 2-D full-field interferometric techniques [1-3, 5, 6]. By either tuning the wavelength or changing the illumination direction, depth information is encoded in the temporal frequencies of the interference signal. This can be thought of as being equivalent to temporal phase shifting by either changing the magnitude or the direction of the illumination wave vector. Fourier transformation along the time axis is then used to reconstruct the object microstructure and to measure phase changes within it.

It is also apparent that these techniques are a form of optical tomography and can be analysed in equivalent terms. The measurement of 3-D structures from interferometric measurement of the scattered field (i.e. holography) was first considered by Wolf [8] and expressed in a frequency space representation [9, 10], while synthesis of 3-D images has been advanced by others [11, 12]. More recently a mathematical framework was proposed that considered holography, tomography and methods of 3-D microscopy as linear filtering operations [13] and this approach will be adopted to compare the depth-resolved, displacement measuring systems that are the subject of this paper.

The following section provides, in chronological order, a brief overview of the phase contrast techniques that have been developed to date to measure internal displacement

fields within weakly scattering transparent materials. Section 3 introduces the theoretical framework in which optical tomography is viewed as a linear filtering operation. Section 4 presents WSI, TSI, PC SOCT and HSI as linear filtering operations focusing on their transfer functions and their associated point spread functions that ultimately determine the spatial resolution and phase sensitivity of the individual techniques.

2. Recent advances on depth-resolved displacement measurements

2.1 Low coherence speckle interferometry (LCSI)

This approach, which can also be regarded as a phase-sensitive version of time-domain OCT, involves the use of a low coherence, i.e. broad spectral bandwidth, light source such as a super luminescent light emitting diode (SLED). As a result, an interference signal is produced only from those parts of the sample where the object and reference wave path lengths are matched to within the coherence length of the light source [14, 15]. 2-D phase difference maps are produced that encode the displacement field for one 'slice' within the sample. By axially moving the illumination beam, different coherent slices can be measured, as schematically shown in Fig. 1 (a). LCSI has some attractive features, in particular experimental simplicity, however an additional scanning device is required to obtain a full 3-D phase volume. Furthermore, the parts of the sample that fall outside the coherence 'gate' contribute a dc offset to the recorded intensity distribution, which reduces significantly the number of gray levels available for detecting the modulation of the interference signal.

2.2 Wavelength-scanning interferometry

In WSI, a setup of which is illustrated in Fig. 1 (b), light scattered by different layers within the material is combined with a reference wave [1, 2]. The optical path difference between object and reference wave varies linearly with the depth of the scattering layer within the sample. Therefore the frequency of the interference signal produced by tuning the wavelength also varies linearly with depth. The signals from different scattering layers can therefore be separated from one another by spectral analysis of the time-varying interference signal measured at each pixel in the image plane. 3-D displacement fields can be determined by measuring phase changes in the

Fourier domain between two successive scans of the sample. WSI has the benefit of a higher signal-to-noise ratio than LCSI, and is intrinsically a 3-D technique. However, a laser source that can tune reliably over an extended wavelength range is required and furthermore the sample needs to be kept mechanically stable for the duration of the scan.

2.3 Tilt-Scanning Interferometry

In TSI, depth-resolved displacements are measured by tilting the illumination angle during the acquisition of image sequences [3]. Figure 1 (c) shows a simplified schematic setup of this technique. The depth-encoding frequency shift can be regarded as coming from the Doppler shift of the photons reflected from the tilting mirror in the object illumination beam path. As in WSI, spectral analysis of the time-varying intensity signal at a given camera pixel provides depth-resolved information, the magnitude relating to the specimen structure and the phase relating to the optical path differences between the scatterers lying within the volume. Figure 2 shows the setup for bending beam experiments, and sample wrapped phase maps from the proof of principle experiments detailed in [3]. The top row shows the horizontal in-plane phase-change distribution for different slices within an epoxy resin beam measured relative to a reference surface at $z = z_1$, starting at the object surface $z - z_1 = 0$ mm (left) in steps of 1.74 mm down to $z - z_1 = 5.22$ mm (right). Good agreement was achieved between the experimentally-determined displacement fields and a finite element model. While TSI has similar stability requirements as WSI, it has the attractive feature of working at a single wavelength, thereby avoiding the need for an expensive tunable laser and side-stepping errors due to dispersion.

2.4 Phase Contrast Spectral OCT

Spectral OCT involves illumination with a sheet of low coherence light extending into the sample from the surface [5, 6]. The intersection of the sheet with the sample forms a line, which is imaged onto a 2-D sensor through a diffraction grating. Figure 1(d) illustrates how it works. The resulting images have one spatial axis and one wavenumber axis, the latter being converted to the depth spatial coordinate by Fourier transformation. As with low-coherence interferometry therefore, some form of scanning is required to measure 3-D volumes. In [5] a method was presented to measure out-of-plane displacement fields from the phase information in the spectral OCT images, and this was extended in [6] to the measurement of both in-plane and out-of-plane displacement fields. An example of the application of the technique to deformation measurement of a porcine cornea after a small change in the intraocular pressure is shown in Fig. 3. The phase change in a cross section of the cornea is encoded as wrapped phase fringes where white represents π and black $-\pi$. In this case the interferometer sensitivity was purely out-of-plane, i.e. the phase is proportional to the corneal displacement along the horizontal direction in Fig. 3. Each fringe corresponds to a displacement of $\sim\lambda/2n$ ~305nm, with n=1.37 the refractive index of the cornea.

2.5 Hyperspectral Interferometry

Hyperspectral interferometry has been recently proposed for the measurement of surface profiles [7]. By using a broad-band light source and a hyperspectral imaging system, a set of interferograms at different wave numbers are recorded simultaneously on a high resolution image sensor. These are then assembled to form a three-dimensional intensity distribution. By Fourier transformation along the wavenumber

axis, an absolute optical path difference is obtained for each pixel independently of the other pixels in the field of view. An example from a proof-of-principle experiment, in which a set of 62 interferograms (three of them enlarged 10×) with a 0.5 nm spectral separation were acquired in a single shot, is shown in Fig. 4, together with the resultant reconstructed surface profile of a 120 μm stepped object. In effect, HSI can be considered to be a full-field single-shot version of spectral OCT, and thus Fig. 1(d) still illustrates the principle behind it, the only difference with PC SOCT being that the imaging system produces a sequence of 2-D images along one axis of the CCD sensor, instead of images of a line on the object. The main limitation of the approach is the limited spatial resolution, however the fact that all the data is acquired simultaneously means that fringe movement due to vibration can be effectively frozen through the use of a sufficiently short exposure duration.

3. 3-D optical imaging as a shift-invariant linear filtering operation

3.1 Tomographic reconstruction

Consider a weakly scattering, non dispersive material of complex refractive index $n'(\mathbf{r}) = n + \Delta n(\mathbf{r})$, with small variations $\Delta n(\mathbf{r})$ around a uniform index n and $\mathbf{r}$ a position vector in 3-D space as shown in Fig. 5. A small volume V in this material, which we will refer to as the object, is illuminated by a plane wave $A_i \exp(i\mathbf{k_i} \cdot \mathbf{r})$ with wave vector $\mathbf{k_i}$ and constant amplitude A_i. The scattered field is measured at a great distance R away from V, much larger than the dimensions of V. Under this far field assumption, this is equivalent to observing the object at a point along the 'observation' wave vector $\mathbf{k_o}$. The object microstructure within V is represented by the scattering potential

$$\Phi(\mathbf{r}) = -(k^2/n^2)\left[2n\Delta n(\mathbf{r}) + \Delta n^2(\mathbf{r})\right], \tag{1}$$

with $k=2\pi/\lambda=|\mathbf{k_o}|=|\mathbf{k_i}|$ the wavenumber associated with the wavelength in the material, related to the vacuum wavelength λ_v by $\lambda=\lambda_v/n$. Using scalar diffraction theory and the previous assumptions it has been shown [9, 16] that the scattered field U observed at $\mathbf{r}\sim R\mathbf{k}_o/|\mathbf{k}_o|$, is given by:

$$U(\mathbf{k_o}) = -\frac{A_i}{4\pi}\frac{\exp(i|\mathbf{k_o}|R)}{R}\int_V \Phi(\mathbf{r}')\exp\left(-i\mathbf{K}\cdot\mathbf{r}'\right)\mathrm{d}^3\mathbf{r}' \tag{2}$$

where $\mathbf{K}/2\pi$ is used as the Fourier variable, with $\mathbf{K}=\mathbf{k_o}-\mathbf{k}_i$ the 'scattering' vector defined in terms of the observation and illumination wave vectors. This equation is a simplified version of the well known theorem of diffraction tomography [17]. Its significance is that the scattered wave is a spherical wave $\exp(i|\mathbf{k_o}|R)/R$ the complex amplitude of which is proportional to the 3-D Fourier transform of the scattering potential. If the illumination consists of a single plane wave of wave vector $\mathbf{k}_i$, all Fourier components of the scattering potential accessible by scattering at different observation directions $\mathbf{k_o}$ are limited to those located on a sphere described by the arrowhead of the scattering vector $\mathbf{K}$. This is known as the Ewald sphere for the specific wavelength λ; it has radius k and is centred at $-\mathbf{k_i}$ (see Fig. 5(b)). If a single illumination and observation direction is used, e.g. speckle interferometry with collimated illumination and observation as illustrated in Fig. 5(a), then a single point in $\mathbf{K}$-space is obtained, labelled A in Fig. 5 (b), which represents a single spatial frequency of the scattering potential. In object-space this corresponds to a plane wave $\exp(-i\mathbf{K}\cdot\mathbf{r})$ which is usually visualized as 3-D parallel sinusoidal fringes known in holography and crystallography as Bragg planes, the normal of which is aligned with $\mathbf{K}$ and the separation or period of which is given by $2\pi/|\mathbf{K}|$. If the object moves by an

amount $\Delta\mathbf{r}$ then the plane wave advances by a phase $\Delta\phi = \mathbf{K}\cdot\Delta\mathbf{r}$. This is the phase change used in speckle interferometry for surface deformation measurements. The **K** vector is recognized here, and from inspection of Fig. 5(a), as the familiar 'sensitivity' vector. We will later come back to comment on the dual meaning of **K** as the 'scattering' and 'sensitivity' vector.

In order to calculate or 'reconstruct' the scattering potential with a certain degree of spatial resolution, the complex amplitude of the scattered field must be measured, for example with an interferometer, over an extended region of **K**-space. Different wave vectors $\mathbf{k_o}$ and $\mathbf{k_i}$ can be combined, by using multiple illumination wavelengths and illumination and observation directions, to populate **K**-space. In general, only a certain portion of K-space is accessible with a given experimental technique, and this region can be regarded as a **K**-space 'window' or 'transfer' function. If we denote $\tilde{\Phi}(\mathbf{K})$ the Fourier transform of the scattering potential $\Phi(\mathbf{r})$, we can express Eq. (2) simply as $U(\mathbf{k_o}) \propto \tilde{\Phi}(\mathbf{K})$, where $\propto$ indicates proportionality. Considering a transfer function $\tilde{G}(\mathbf{k_o})$ that accounts for the observation directions $\mathbf{k_o}$ at which the 'measured' field U_m is obtained:

$$U_m(\mathbf{k_o}) = U(\mathbf{k_o})\,\tilde{G}(\mathbf{k_o}) \;\propto\; \tilde{\Phi}(\mathbf{K})\,\tilde{G}(\mathbf{k_o}) \;. \qquad (3)$$

It is convenient now to: 1) replace $\mathbf{k_o}$ by **K** in the left hand side of Eq. (3), as this just represents a **K**-space coordinate; 2) to write $\tilde{G}(\mathbf{k_o})$ in the right hand side as a transfer function in the variable $\mathbf{K}+\mathbf{k_i}$; and 3) to define a new transfer function $\tilde{H}(\mathbf{K}) = \tilde{G}(\mathbf{K}+\mathbf{k_i})$ that is a shifted version of $\tilde{G}(\mathbf{K})$ by $-\mathbf{k_i}$. Therefore Eq. (3) reduces to:

$$U_m(\mathbf{K}) \propto \tilde{\Phi}(\mathbf{K})\,\tilde{\mathrm{H}}(\mathbf{K}) \ , \tag{4}$$

The convolution theorem allows us to write Eq. (4) in terms of the 'reconstructed' object, $\tilde{U}_m(\mathbf{r})=FT^{-1}\{U_m(\mathbf{K})\}$, the impulse response of the system, $\mathrm{H}(\mathbf{r}) = FT^{-1}\{\tilde{\mathrm{H}}(\mathbf{K})\}$, and the scattering potential. If $\otimes$ denotes convolution, then

$$\tilde{U}_m(\mathbf{r}) = \Phi(\mathbf{r}) \otimes \mathrm{H}(\mathbf{r}) \ . \tag{5}$$

Equations (4) and (5) express the reconstruction problem as a linear, shift invariant, filtering operation [13]. H(**r**) is a key function for all the depth-resolving techniques since it determines their spatial resolution and sensitivity. We therefore now consider how to evaluate this function on a case-by-case basis.

3.1 Monochromatic optical tomography

Each of the depth-resolved methods described in section 2 are interferometric and are analogous to holographic methods that measure both the phase and amplitude of the scattered field. In common with all far-field optical instruments, however, they only collect a fraction of the scattered field by the entrance pupil, defined by the object-space numerical aperture of the system $\mathrm{N_A}= n \sin(\alpha)$ where α is the half-angle subtended by the cone of rays accepted by the aperture from a point in the object. It has been shown in [13] that when an axially symmetric system with finite $\mathrm{N_A}$ is used to measure the complex scattered field, the transfer function can be written as

$$\tilde{G}_{NA}(\mathbf{K}) = \frac{\delta\left(|\mathbf{K}| - k\right)}{k^2} \text{step}\left[\mathbf{K}\cdot\hat{\mathbf{n}}_o - k\sqrt{1-N_A^2}\right], \quad (6)$$

where step(x) is the Heaviside step function. This corresponds to a portion of a sphere of radius k and centred at the origin of **K**-space, indicated in Eq. (6) by the Dirac delta function. It is clear that the finite N_A places a restriction on the wave vectors accepted by the system and this constraint is manifest in the term $\text{step}\left[\mathbf{K}\cdot\hat{\mathbf{n}}_o - k\sqrt{1-N_A^2}\right]$ where $\hat{\mathbf{n}}_o$ is a unit vector along the observation axis (see Fig. 6). To find the impulse response we notice that the scattering potential, as defined before, includes a factor k^2. On the other hand, the transfer function $\tilde{G}_{NA}(\mathbf{K})$ in Eq. (6) includes a normalization factor $1/k^2$. When the object is illuminated by a wave vector $\mathbf{k_i}$ the transfer function for reconstruction can be conveniently expressed as a version of $\tilde{G}_{NA}(\mathbf{K})$ shifted by $-\mathbf{k_i}$: $\tilde{H}_{NA}(\mathbf{K}) = k^2\tilde{G}_{NA}(\mathbf{K}+\mathbf{k_i})$. Finally, we can define an 'object function' $O(\mathbf{r}) = \Phi(\mathbf{r})/k^2$ that represents the object microstructure and is independent of the wavelength used to reconstruct it. From Eqs. (4) and (5), this leads to a simple expression for the reconstructed object:

$$\tilde{U}_m(\mathbf{r}) = O(\mathbf{r}) \otimes H_{NA}(\mathbf{r}). \quad (7)$$

Thus, tomographic reconstruction using a monochromatic single plane wave illumination can be summarized as a linear filtering operation with transfer function $\tilde{H}_{NA}(\mathbf{K})$ and impulse response $H_{NA}(\mathbf{r})$. Figure 6(b) shows the transfer function and 6(c) indicates the axial and lateral bandwidths:

$$\Delta k_z = k(1-\sqrt{1-\mathrm{N_A}^2}) \approx \frac{1}{2} k\mathrm{N_A}^2$$

$$\Delta k_{x,y} = 2k\mathrm{N_A} \tag{8}$$

The significance of these **K**-space bandwidths lies in the fact that the impulse response, i.e. the resolution, of the tomographic imaging systems is inversely proportional to them. For a rectangular transfer function with bandwidths Δk_x, Δk_y and Δk_z, and uniform power spectral density in **K**-space, the extent of the impulse response along *x*-, *y*- and *z*-axes, measured as the distance between first zero-crossing points is given by:

$$\delta x = \gamma \frac{2\pi}{\Delta k_x}; \quad \delta y = \gamma \frac{2\pi}{\Delta k_y}; \quad \delta z = \gamma \frac{2\pi}{\Delta k_z}, \tag{9}$$

with $\gamma = 2$. If the power distribution in **K**-space is not uniform, then the width of the peak is broadened by a factor $\gamma > 2$ that depends on the specific spectral power density. In 1-D, this is equivalent to windowing the signal, for example using Hanning window. An extended transfer function as in this case has associated with it a mean scattering or sensitivity vector $\langle \mathbf{K} \rangle$ which points to the centroid of the transfer function as shown in Fig. 6(c).

Eqs. (9) can be used to estimate, from the extension of the transfer function in **K**-space, the axial and lateral depth resolutions. We consider here the maximum overall bandwidth along k_x or k_z, essentially defined by the bounding box of the transfer function. Due to the lesser contribution of those spatial frequencies at opposed corners of the 'diamond', this figure will not be achieved in practice (γ will be greater than 2) and should be taken as an absolute theoretical maximum.

4. K-space representation of depth-resolved displacement measurement techniques

4.1 WSI, HSI and PC SOCT

We will see that WSI, PC-SOCT and HSI are all equivalent in terms of their representation in **K**-space, regardless of the differences in their practical implementation as described in Sections 2.2, 2.4 and 2.5. The reconstructed object microstructure $\tilde{U}_{WSI}(\mathbf{r})$ (valid also for PC-SOCT and HSI) is simply the superposition of all the instantaneous monochromatic optical tomography reconstructions for all the different illumination wavelengths $\lambda_2 < \lambda < \lambda_1$ within the source spectral range $\Delta\lambda = \lambda_1 - \lambda_2$, when the illumination direction remains fixed. In terms of wave vectors, this is equivalent to a scan of $|\mathbf{k}_i|$ between $k_1=k_0-\Delta k/2$ and $k_2=k_0+\Delta k/2$ with $\Delta k = 2\pi[(1/\lambda_1)-(1/\lambda_2)]$ and k_0 the central wavenumber. According to Eq. (43):

$$U_{WSI}(\mathbf{K}) = \tilde{\mathrm{O}}(\mathbf{K})\tilde{\mathrm{H}}_{WSI}(\mathbf{K}) \tag{10}$$

with transfer function

$$\tilde{\mathrm{H}}_{WSI}(\mathbf{K}) = \int_{k_1}^{k_2} k^2 S(k)\tilde{\mathrm{G}}_{NA}(\mathbf{K}+\hat{\mathbf{n}}_i k)dk \tag{11}$$

and where $S(k)$ is the amplitude spectral density of the light source. Figure 7(a) shows a schematic setup of WSI with normal collimated illumination and observation with a

finite numerical aperture N_A. Figure 7(b) shows the Ewald sphere representation in **K**-space of the transfer function corresponding to the WSI system depicted in Fig. 7(a). For simplicity, only the plane with axes k_x, k_z is shown in the figure. To aid with the geometric construction, two spheres are indicated corresponding to wave numbers k_1 and k_2 ($k_1<k_2$). The transfer function is shown again in Fig. 7(c) with the effective sensitivity vector $\langle \mathbf{K} \rangle$.

Similarly, Fig. 8(a) shows a schematic setup of PC-SOCT with dual sensitivity [5]. In this case the object is illuminated sequentially from both sides on the plane *xz* to achieve different sensitivities but the same spatial resolution for each illumination direction. The transfer function corresponding to left illumination is shown in Fig. 8(b). Figure 8(c) shows the transfer functions and effective sensitivity vectors $\langle \mathbf{K_1} \rangle$ and $\langle \mathbf{K_2} \rangle$ obtained if left and right illumination directions are used sequentially. In-plane and out-of-plane sensitivities are achieved by combining the phase obtained from the 3-D Fourier transforms of the transfer functions corresponding to each illumination direction.

The transfer functions depicted in Figs. 7(b)-(c) and 8(b)-(c) define what spatial frequencies in the object can be captured by the depth-resolved imaging system. In the k_x, k_y plane, not depicted here, the transfer function is simply a circle representing the input aperture of the imaging lens, its radius representing the maximum transverse spatial frequencies allowed. Figure 9(a) illustrates the transfer function for WSI, PC-SOCT and HSI for different illumination directions, $N_A = 0.04$ and $\Delta k/k_0 = 0.1$ in a **K**-space normalized by k_0. From the dimensions of the transfer function 'diamond', it can be shown that for a WSI, PC-SOCT or HSI system with numerical aperture N_A, illumination angle θ and source spectral bandwidth Δk between k_1 and k_2, the bandwidths of the transfer function in the axial and lateral directions are given by:

$$\Delta k_z \approx \begin{cases} \frac{1}{2} k_2 \mathrm{N_A}^2 & \text{for } \left|1+\cos\theta\right| < \frac{\mathrm{N_A}^2}{2} \\ \frac{1}{2} k_1 \mathrm{N_A}^2 + \Delta k(1+\cos\theta) & \text{otherwise} \end{cases} \tag{12}$$

$$\Delta k_x \simeq \begin{cases} \Delta k \left|\sin\theta\right| + (k_1 + k_2)\mathrm{N_A} & \text{for } \left|\sin\theta\right| > 2\mathrm{N_A} \\ 2k_2 \mathrm{N_A} & \text{otherwise} \end{cases} \tag{13}$$

$$\Delta k_y \simeq 2k_1 \mathrm{N_A} \tag{14}$$

Figure 9(b) shows a plot of the above equations (normalized to the central wavenumber k_0) for illumination angles $0 \le \theta < 2\pi$ in the plane xz in Fig. 8(a), for N_A=0.04 and $\Delta k/k_0$ =0.1. The horizontal and vertical axes correspond to **K**-space directions k_x and k_z. Note the constant value of Δk_y for all θ. The axial bandwidth, that is inversely related to the depth resolution, is maximum for normal illumination and minimum for transmission, as expected. The lateral bandwidth Δk_x increases with increasing illumination angles except around normal illumination, where it is the same as Δk_y.

Figure 10 shows the positive values of the real part of the impulse response in the plane xz corresponding to different transfer functions as indicated in Fig. 9(a) for various illumination directions, N_A=0.04 and $\Delta k/k_0$ =0.1. Fig. 10(a) shows the impulse response for the case of $\theta = 0$ (backscattering). The cosinusoidal fringes in the real part of the impulse response are important because they can be regarded as being responsible for the phase sensitivity of the technique. A displacement $\Delta\mathbf{r}$ of a point

source will produce a phase change $\Delta\phi = \langle \mathbf{K} \rangle \cdot \Delta \mathbf{r}$ in the reconstruction of that point. The *x* and *z* axes are normalized to the central wavelength λ_0. Figure 10(b) shows again the real part of the impulse response, this time for an illumination angle $\theta_c = \pi/2$. Figures 10 (c) and (d) correspond to the case when $\theta_c = -\pi/4$ and $\pi/4$, respectively. These symmetric illuminations lead to fringes across the impulse response of equal spacing but opposite orientations. The addition and subtraction of the phase changes measured in each case after object deformation enables the measurement of out-of-plane and in-plane displacements, respectively.

4.2 Tilt-Scanning Interferometry

Similar to the WSI case, the reconstructed object microstructure in TSI, $\tilde{U}_{TSI}(\mathbf{r})$, results from the superposition of the individual monochromatic optical tomography reconstructions for all the different illumination directions $\mathbf{k}_i = -\frac{2\pi}{\lambda}\hat{\mathbf{n}}_i$, with $\hat{\mathbf{n}}_i = \sin\theta\,\hat{\mathbf{i}} + \cos\theta\,\hat{\mathbf{k}}$ a unit vector subtending an angle θ to the *z*-axis inside the material. According to Eq. (4):

$$U_{TSI}(\mathbf{K}) = \tilde{O}(\mathbf{K})\,\tilde{H}_{TSI}(\mathbf{K}) \tag{15}$$

with transfer function

$$\tilde{H}_{TSI}(\mathbf{k}) = k^2 \int_{\theta_c-\Delta\theta/2}^{\theta_c+\Delta\theta/2} \Theta(\theta)\tilde{G}_{NA}\left[\mathbf{K} + k(\sin\theta\,\hat{\mathbf{i}} + \cos\theta\,\hat{\mathbf{k}})\right] d\theta \tag{16}$$

where $\Theta(\theta)$ is the angular density of the measurements and is usually approximately constant. Figure 11(a) shows a schematic view of a TSI optical setup, where interferograms with left and right illumination directions are recorded in sequence. Figure 11(b) shows a 2-D slice of **K**-space with the illumination, observation, and scattering vectors. The angle θ of the illumination wave vector $\mathbf{k}_i$ changes sequentially around a central value θ_c. The tilting range $\Delta\theta$ is also indicated. The observation wave vectors $\mathbf{k_o}$ lie within a cone that is captured by the imaging lens of the system, characterized by the numerical aperture. The transfer function represents all the possible spatial frequencies that are captured by the system and is given by the superposition of the scattering vectors $\mathbf{K}=\mathbf{k_o}-\mathbf{k_i}$. Figure 11(b) shows graphically the sum of vectors $-\mathbf{k_i}$ and all possible $\mathbf{k_o}$. For a single illumination direction, this corresponds to wave vectors lying on a spherical shell of radius k but shifted by the illumination wave vector $-\mathbf{k}_i$. Multiple illumination directions have the effect of spreading this transfer function into a 'diamond' shape region. The sensitivity vectors for left and right illuminations, $\langle\mathbf{K_1}\rangle$ and $\langle\mathbf{K_2}\rangle$, point to the centroid of their respective transfer functions, as shown in Fig. 11(c). By adding and subtracting phases $\langle\mathbf{K_1}\rangle\cdot\mathbf{r}$ and $\langle\mathbf{K_2}\rangle\cdot\mathbf{r}$, the out-of-plane and in-plane sensitivities are obtained, respectively. The axial and lateral bandwidths Δk_z and Δk_x are indicated in Fig. 11(c), and these ultimately determine the axial and lateral spatial resolutions. Note how the Ewald spheres that correspond to the maximum and minimum illumination angles, bound the spatial frequencies that are measured with the TSI system.

Figure 12(a) illustrates the transfer function for TSI for different central illumination directions θ_c, N_A = 0.04 and $\Delta\theta$ = 0.2 rad in a **K**-space normalized by k. From the geometry depicted it can be shown that for a TSI system with numerical aperture N_A

and illumination angle ranging from θ_1 to θ_2 ($\theta_1 < \theta_2$) the bandwidths of the transfer function in the axial and lateral dimensions are given by

$$\Delta k_z \approx \begin{cases} \frac{1}{2} k\mathrm{N_A}^2 + k(1 - \min(|\cos\theta_2| - |\cos\theta_1|) & \begin{cases} \text{for } \theta_2 > 0 \;\&\; \theta_1 < 0 \\ \text{or } -\pi < \theta_2 < 0 \;\&\; \frac{\pi}{2} < \theta_1 < \pi \end{cases} \\ \frac{1}{2} k\mathrm{N_A}^2 + k\left|\cos\theta_2 - \cos\theta_1\right| & \text{otherwise} \end{cases} \tag{17}$$

$$\Delta k_x \approx \begin{cases} 2k\mathrm{N_A} + k(1 - \min(|\sin\theta_2| - |\sin\theta_1|) & \begin{cases} \text{for } \theta_2 > \frac{\pi}{2} \;\&\; \theta_1 < \frac{\pi}{2} \\ \text{or } \theta_2 > -\frac{\pi}{2} \;\&\; \theta_1 < -\frac{\pi}{2} \end{cases} \\ 2k\mathrm{N_A} + k\left|\sin\theta_2 - \sin\theta_1\right| & \text{otherwise} \end{cases} \tag{18}$$

$$\Delta k_y \approx 2k\mathrm{N_A} \tag{19}$$

Figure 12(b) shows a plot of the above equations for all possible central illumination angles θ_c in the plane *xz*, for N_A=0.04 and an illumination angle range $\Delta\theta$=0.2 rad. The axial bandwidth is minimum for normal illumination and maximum at $\theta_c=\pm\pi/2$. It does not reach the origin for $\theta_c=\pm\pi$, the minimum bandwidth in that case being due to the N_A of the system, according to Eq. (17). The lateral bandwidth Δk_x decreases with increasing illumination angles, and at $\theta_c=\pm\pi/2$ it is the same as Δk_y, which remains constant for all θ_c.

Figure 13 shows the magnitude and the real part of the impulse response in the plane *xz* corresponding to different transfer functions for a TSI system as indicated in Fig. 10 (a) for various central illumination directions, N_A=0.04 and $\Delta\theta$=0.2 rad.

5. Discussion

In general terms, a transfer function $\tilde{H}(\mathbf{K})$ centred at the origin (e.g. due to forward scattering, results in an impulse response $H(\mathbf{r})$ with nearly no phase gradient (see Fig. 14 (a)). The spatial extent of the impulse response defines the resolution of the 3-D image according to Eqn. (9). The effect of shifting $\tilde{H}(\mathbf{K})$ from the origin by a wave vector $\langle\mathbf{K}\rangle$ is to add a phase term to the impulse response. This is expressed by the Fourier transform shift theorem: $FT\{\tilde{H}(\mathbf{K}-\langle\mathbf{K}\rangle)\}(\mathbf{r}) = \exp(-i\langle\mathbf{K}\rangle\cdot\mathbf{r})H(\mathbf{r})$, from which it is clear also that the vector $\langle\mathbf{K}\rangle$ is the phase gradient within the impulse response (see Fig. 14 (b)). For the measurement of deformation, this phase variation within the impulse response has a greater significance linked to the view of $\langle\mathbf{K}\rangle$ as the sensitivity vector. If the object is deformed such that an individual scattering particle moves, its image (or reconstruction) will move in unison. Measurement of the phase change at a given point can be used to determine the object displacement along $\langle\mathbf{K}\rangle$.

The interpretation of optical tomography as a linear filtering operation provides a powerful tool to compare the relative advantages and limitations of different systems. Even though they may differ considerably in their physical implementation, all the methods reviewed and some others in the literature reduce to different strategies to populate **K**-space. Whereas WSI, PC SOCT and HSI rely on the source spectral bandwidth to increase the depth resolution, TSI relies on the width of the angular scan. It is clear from Fig. 12 (a) that the maximum depth resolution in TSI is achieved for a central illumination angle $\theta_c=\pi/2$ (only viable in certain cases depending on the object studied). This illumination direction is also interesting because it results in an axially symmetric impulse response and equal in-plane and out-of-plane sensitivities.

There are other realizations of TSI: in biology, Lauer microscopy is used to produce tomographic views of cells [13, 18]. In a backscattering configuration this is essentially the same as TSI, the only difference being that in TSI the central angle is non zero, which greatly increases depth resolution and also allows the separation of in-plane and out-of-plane sensitivity by combining phase measurements obtained for different illumination directions, symmetric with respect to the observation direction. Another technique known as angular spectrum scanning, essentially TSI but using a spatially incoherent ring source of variable radius, was used successfully in 2-D absolute distance profilometry [19].

It should be pointed out that there are some limitations to the model presented here which could be improved in the future. We have found upper bounds to the bandwidths of the transfer functions in all axes in **K**-space. A better estimate for the spatial resolution could be achieved by computing geometric moments of the transfer functions, to account for the 'diamond' shape and for the non uniform power density in **K**-space.

We also limited the discussion to the case in which the illumination and observation are done within a material medium in which small variations of refractive index exist. In real applications, however, an air/material interface is often present (e.g. air/epoxy, air/cornea) and the illumination and observation directions set by the optical system do not correspond to the $\mathbf{k_i}$ and $\mathbf{k_o}$ vectors within the material. This refraction effect has multiple consequences; while lateral resolution and sensitivity remain unchanged, axial resolution decreases within the medium in proportion to its mean refractive index *n*. Moreover, the axial displacement sensitivity increases in proportion to the mean refractive index. Refraction at curved interfaces leads to distortions of the

reconstructed object, which can be minimized by immersing the sample in a cell with index matching fluid and looking through a flat window.

In backscatter WSI, PC-SOCT and HSI the numerical aperture of the imaging system controls the lateral resolution. At oblique incidence, the illumination angle can become dominant for small numerical apertures, however, the angular bandwidth of the illumination also has a great influence. For example, scanning white light interferometry (SWLI) [20] which is commonly used for profilometry, uses a broad angular spectrum for the illumination to double the lateral resolution. Depth resolution is controlled by a combination of spectral and angular bandwidths according to Eqn. (12). In the case of SWLI the depth resolution is dominated by the angular bandwidth when objective lenses of high numerical aperture are used, and this is the sole cause of high depth resolution in monochromatic confocal microscopy [21]. In WSI, PC-SOCT and HSI lenses of small numerical aperture are commonly used, and the dominant parameter that controls the depth resolution is the spectral bandwidth of the light source.

In comparison, both the lateral and depth resolution in TSI depend strongly on the tilting range and the central illumination angle. In the special case of a 90 degree illumination angle, the tilting range has no effect on the lateral resolution and is solely due to the numerical aperture, while the depth resolution is determined by the tilting range.

6. Conclusions

A family of techniques recently developed for high sensitivity depth-resolved measurements in semitransparent scattering materials were presented within a

common framework that represents optical tomographic methods as linear filtering operations. WSI, PCSOCT, HSI and TSI were all expressed in terms of their transfer functions in **K**-space, which provides direct information on the accessible spatial frequencies in the object microstructure given certain illumination and observation directions and the spectral bandwidth of the light source. The reconstructed object microstructure is simply the convolution of the object function and the impulse response of the system. Phase sensitivity, used for the determination of 3-D distribution of displacement fields, is determined by the phase gradient within the impulse response function, given by the average scattering vector $\langle \mathbf{K} \rangle$.

7. Acknowledgments

This work was supported in part by the Engineering and Physical Sciences Research Council, UK, grant numbers EP/E050565/1 and EP/F02861X/1.

Figure Captions

Fig. 1 Different techniques have been used to measure displacement fields with phase sensitivity: a) Low Coherence Speckle Interferometry; b) Wavelength Scanning Interferometry; c) Tilt Scanning Interferometry and d) phase contrast Spectral Optical Coherence Tomography and Hyperspectral Interferometry. BS: beam splitter, SLED: super luminescent light emitting diode, O: object, CCD: charged coupled device photodetector array, G: diffraction grating, TS: translation stage.

Fig. 2 Left: Schematic view of an epoxy resin beam undergoing 3-point bending; Right: in-plane (top row) and out-of-plane (bottom row) wrapped phase-change distribution for different slices within the beam. Black represents $-\pi$ and white $+\pi$. Fringe spacing is equivalent to ~0.38μm and ~0.15μm for in-plane and out-of-plane sensitivity, respectively.

Fig. 3 Phase change measured on a slice through porcine cornea after a change in the intraocular pressure.

Fig. 4 Single shot 2-D profilometry using Hyperspectral Interferometry. Left: 62 interferograms (0.5 nm separation) of stepped surface and (inset) 3 enlarged images; Right: reconstructed surface profile of the stepped surface.

Fig. 5 K-space representation of illumination and scattered fields for optical tomography: a) Collimated monochromatic illumination and detection; b) Scattering or sensitivity vector **K** corresponding to the system shown in (a).

Fig. 6 Monochromatic optical tomography: a) optical setup with normal collimated illumination and observation with a finite numerical aperture N_A; b) Ewald sphere representation in **K**-space of the transfer function corresponding to the system depicted in a); c) Transfer function spectral bandwidths and sensitivity vector.

Fig. 7 Wavelength Scanning Interferometry: a) optical setup with normal collimated illumination and observation with a finite numerical aperture N_A; b) Ewald sphere representation in **K**-space of the transfer function corresponding to the system depicted in a); c) Transfer function and sensitivity vector.

Fig. 8 Phase Contrast Spectral Optical Coherence Tomography with dual sensitivity: a) optical setup with collimated oblique illumination from both left and right sides and observation with a finite numerical aperture N_A; b) Ewald sphere representation in **K**-space of the transfer function corresponding to the left illumination shown in a); c) Transfer functions and sensitivity vectors obtained if left and right illumination directions are used sequentially. Both in-plane and out-of-plane sensitivities are achieved by combining the phase obtained from the 3-D FFT of each transfer function diamond.

Fig. 9 a) Simulated transfer functions (**K**-space coordinates normalized to k_0) obtained for WSI, PC-SOCT and HSI systems for different illumination directions. (k_x, k_z) ~ (0, 2) at the top corresponds to $\theta = 0$ (backscattering). Then, moving counter-clock-wise, $\theta = \pi/4, \pi/2, 3\pi/4, \pi$ (transmission), $5\pi/4, 3\pi/2$ and $7\pi/4$. In all these cases, $N_A = 0.04$ and $\Delta k/k_0 = 0.1$. b) Bandwidth of the transfer function of a WSI system as a function of the illumination angle θ in the *xz* plane.

Fig. 10 Positive values of the real part of the impulse response sections at plane *xz* obtained for N_A=0.4 and $\Delta k/k_0 = 0.1$ at different illumination directions for a WSI system: a) θ=0 (backscattering), b) θ=$\pi/2$, c) θ=-$\pi/4$, d) θ=$\pi/4$.

Fig. 11 Tilt Scanning Interferometry: a) optical setup with collimated illumination tilted an angle $\Delta\theta$ around θ_c, and observation with a finite numerical aperture N_A; b) Ewald sphere representation in **K**-space of the transfer function corresponding to the left illumination shown in a); c) Transfer functions and sensitivity vectors obtained if

left and right illumination directions are used sequentially. Both in-plane ($\mathbf{K}_x$) and out-of-plane ($\mathbf{K}_z$) sensitivities are achieved by combining the phase obtained from the 3-D FFT of each transfer function 'diamond'.

Fig. 12 Simulated transfer functions (**K**-space coordinates normalized to *k*) obtained for TSI for different centre illumination directions: a) (k_x, k_z) ~ (0, 2) at the top corresponds to $\theta_c = 0$ (backscattering). Then, moving counter-clock-wise, $\theta = \pi/4, \pi/2, 3\pi/4, \pi$ (transmission), $5\pi/4$, $3\pi/2$ and $7\pi/4$. In all cases, $N_A = 0.04$ and $\Delta\theta = 0.2$ rad. b) Bandwidths of the transfer function of a TSI system as a function of the centre illumination angle θ_c in the *xz* plane.

Fig. 13 Positive values of the real part of the impulse response sections at plane *xz* obtained for $N_A=0.4$, $\Delta\theta=0.2$ rad and different illumination directions (rad) for a TSI system: a) $\theta_c=0$ (backscattering), b) $\theta_c = \pi/2$, c) $\theta_c = -\pi/4$, d) $\theta_c=\pi/4$.

Fig. 14 Fourier shift theorem and the sensitivity vector: a) A general transfer function centred at the origin in K-space (left) has an associated complex impulse response, the magnitude, phase, and real and imaginary parts of which are shown schematically (right). b) When the transfer function is shifted from the origin by $\langle\mathbf{K}\rangle$, the scattering vector corresponding to the centroid of the transfer function, the impulse response has the same spatial extent but now includes a phase gradient $\langle\mathbf{K}\rangle$, which becomes the sensitivity vector of the system.

References

1. Ruiz, P.D., et al., *Depth-resolved whole-field displacement measurement using wavelength scanning interferometry.* Journal of Optics A: Pure and Applied Optics, 2004. **6**(7): p. 679-683.
2. Ruiz, P.D., J.M. Huntley, and R.D. Wildman, *Depth-resolved whole-field displacement measurement by wavelength-scanning electronic speckle pattern interferometry.* Applied Optics, 2005. **44**(19): p. 3945-3953.
3. Ruiz, P.D., J.M. Huntley, and A. Maranon, *Tilt scanning interferometry: a novel technique for mapping structure and three-dimensional displacement fields within optically scattering media.* Proceedings of the Royal Society A-Mathematical Physical and Engineering Sciences, 2006. **462**(2072): p. 2481-2502.
4. Galizzi, G.E., P.D. Ruiz, and G.H. Kaufmann, *Tilt scanning interferometry: a numerical simulation benchmark for 3D metrology.* Applied Optics, 2009. **48**(17): p. 3184-3191.
5. De la Torre-Ibarra, M.H., P.D. Ruiz, and J.M. Huntley, *Double-shot depth-resolved displacement field measurement using phase-contrast spectral optical coherence tomography.* OPTICS EXPRESS, 2006. **14**(21): p. 9643-9656.
6. Ibarra, M.H.D., P.D. Ruiz, and J.M. Huntley, *Simultaneous measurement of in-plane and out-of-plane displacement fields in scattering media using phase-contrast spectral optical coherence tomography.* Optics Letters, 2009. **34**(6): p. 806-808.
7. Huntley, J.M., T. Widjanarko, and P.D. Ruiz, *Hyperspectral interferometry for single-shot absolute measurement of two-dimensional optical path distributions.* Measurement Science and Technology, 2010 (in press).
8. Wolf, E., *Three-dimensional structure determination of semi-transparent objects from holographic data.* Opt. Comm, 1969. **1**(4): p. 153-156.
9. Fercher, A.F., et al., *Image-Formation by Inversion of Scattered Field Data - Experiments and Computational Simulation.* Applied Optics, 1979. **18**(14): p. 2427-2439.
10. Dändliker, R. and K. Weiss, *Reconstruction of the three-dimensional refractive index from scattered waves.* Optics Communications, 1970. **1**(7): p. 323-328.
11. Fercher, A.F., et al., *Optical coherence tomography - principles and applications.* Reports on Progress in Physics, 2003. **66**(2): p. 239-303.
12. Kak, A.C. and M. Slaney, *Principles of Computerized Tomographic Imaging*. 1988: IEEE Press.
13. Coupland, J.M. and J. Lobera, *Holography, tomography and 3D microscopy as linear filtering operations.* Measurement Science & Technology, 2008. **19**(7): p. 070101.
14. Gülker, G. and A. Kraft. *Low-coherence ESPI in the investigation of ancient terracotta warriors*. in *Speckle Metrology 2003*. 2003. Trondheim, Norway: SPIE.
15. Gastinger, K., S. Winther, and K.D. Hinsch. *Low-coherence speckle interferometer (LCSI) for characterization of adhesion in adhesive-bonded joints*. in *Speckle Metrology 2003*. 2003. Trondheim, Norway: SPIE.

16. Fercher, A.F., et al., *Measurement of intraocular distances by backscattering spectral interferometry.* Opt. Comm, 1995. **117**: p. 43-48.
17. Born, M. and E. Wolf, *Principles of optics : Electromagnetic theory of propagation, interference and diffraction of light*. seventh ed. 1999, London: Cambridge University Press.
18. Lauer, V., *New approach to optical diffraction tomography yielding a vector equation of diffraction tomography and a novel tomographic microscope.* Journal of Microscopy 2002. **205**: p. 165-176.
19. Duan, Z.H., Y. Miyamoto, and M. Takeda, *Dispersion-free optical coherence depth sensing with a spatial frequency comb generated by an angular spectrum modulator.* OPTICS EXPRESS, 2006. **14**(25): p. 12109-12121.
20. Deck, L. and P. de Groot, *High-speed noncontact profiler based on scanning white-light interferometry.* Appl. Opt., 1994. **33**(31): p. 7334-7338.
21. Minsky, M., *Memoir on inventing the confocal scanning microscope.* Scanning, 1988. **10**.

Fig1
Click here to download Figure: Fig1.doc

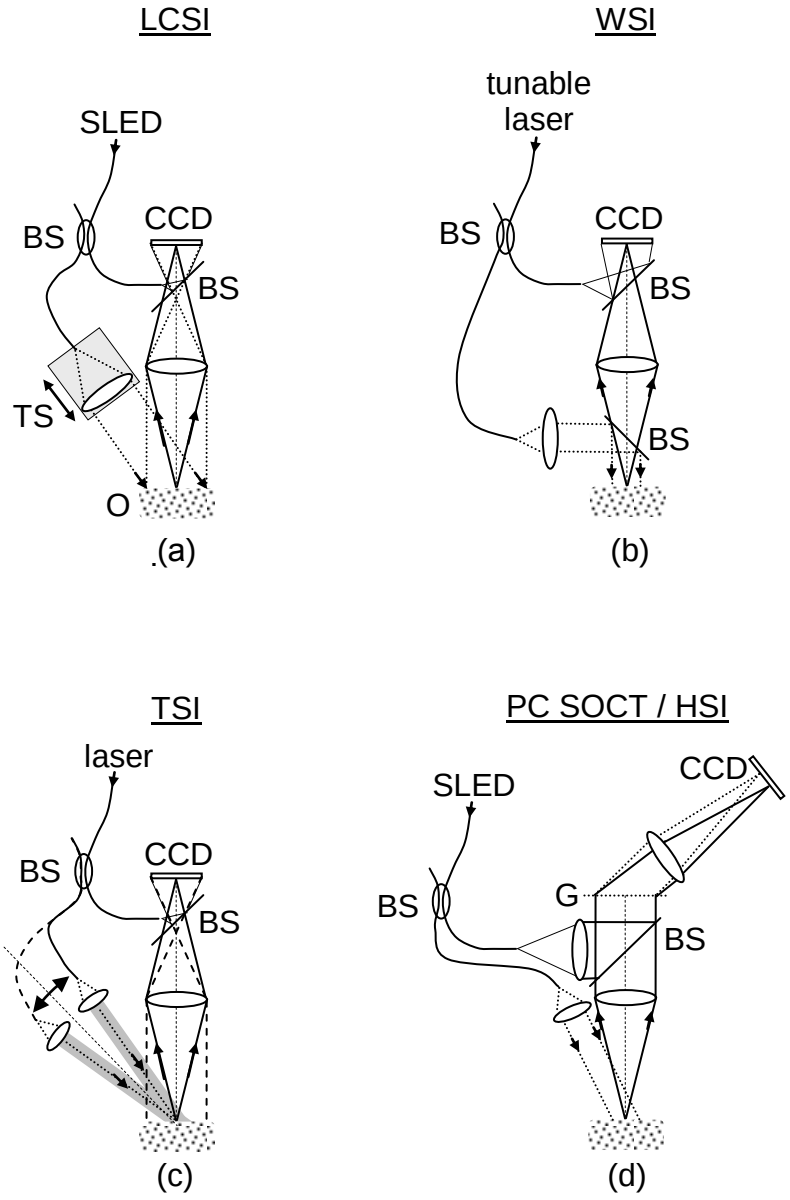

Fig. 1

Fig2
Click here to download Figure: Fig2.doc

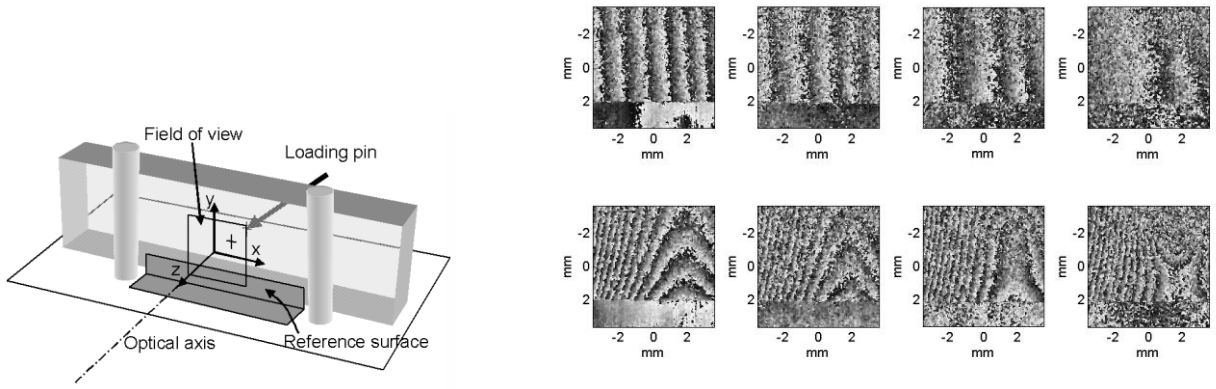

Fig. 2

Fig3

Click here to download high resolution image

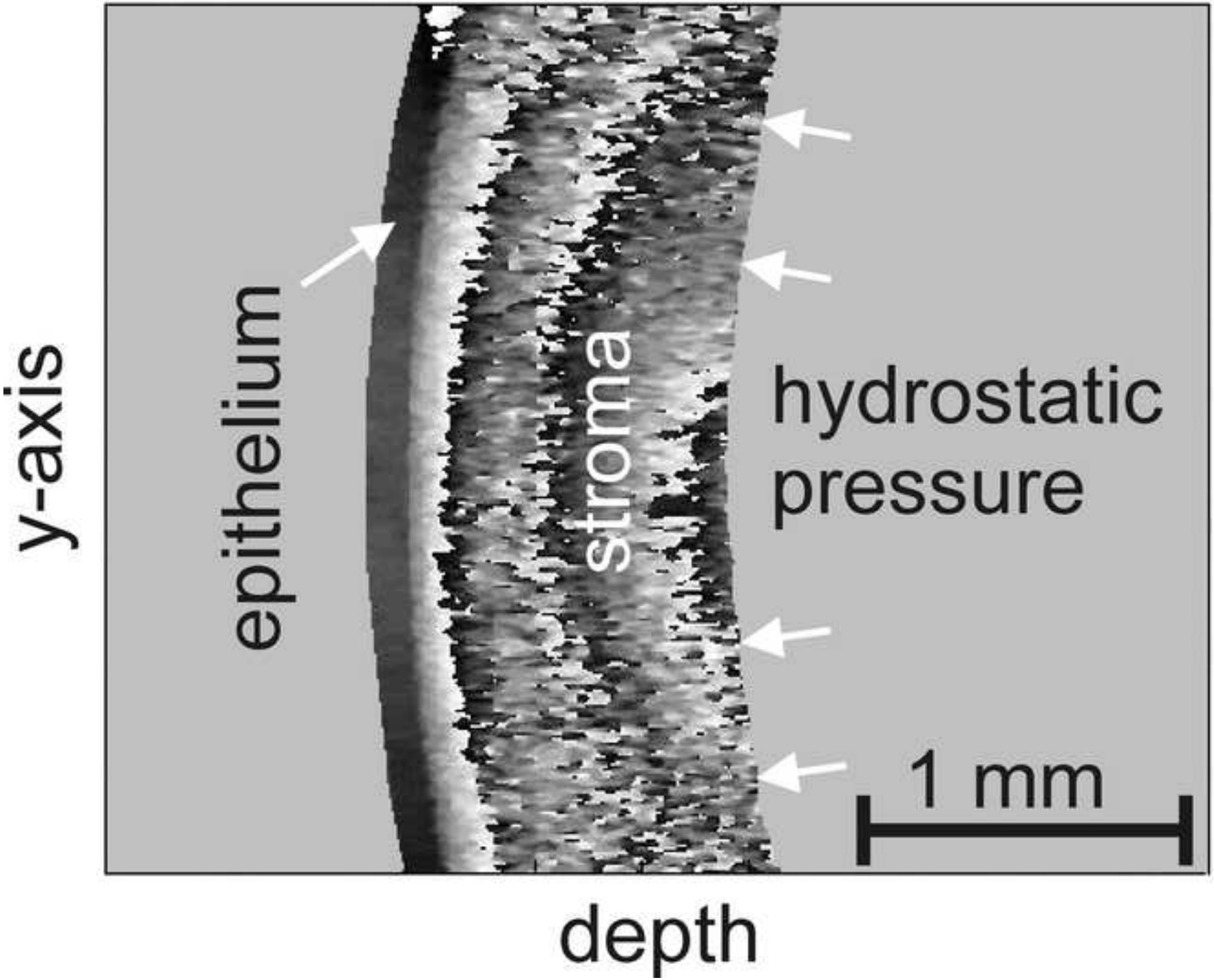

Fig4
Click here to download Figure: Fig4.doc

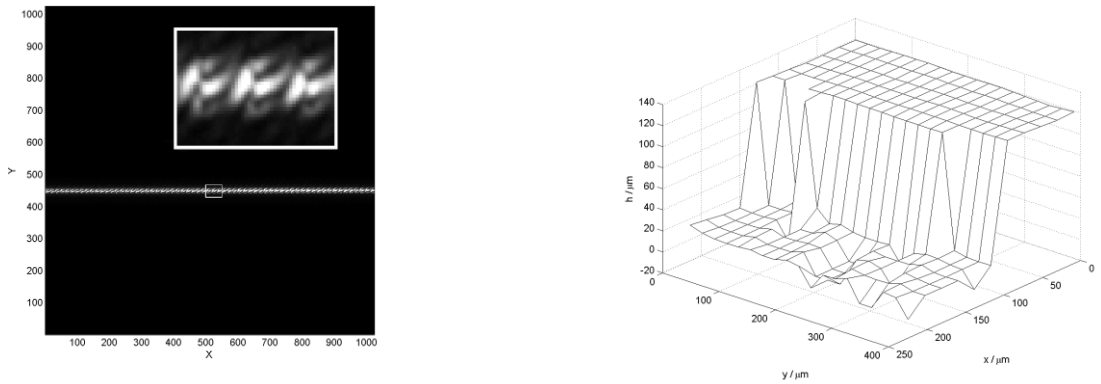

Fig. 4

Fig5
Click here to download Figure: Fig5.doc

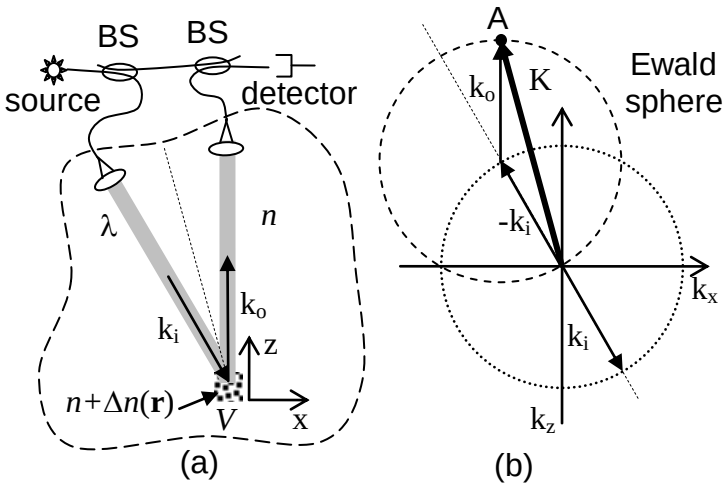

Fig. 5

Fig6
Click here to download Figure: Fig6.doc

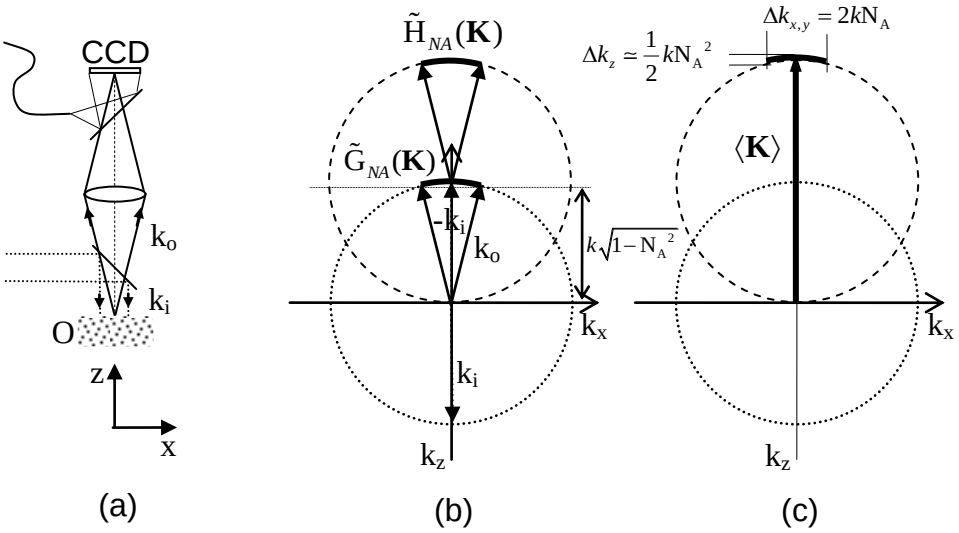

Fig. 6

Fig7
Click here to download Figure: Fig7.doc

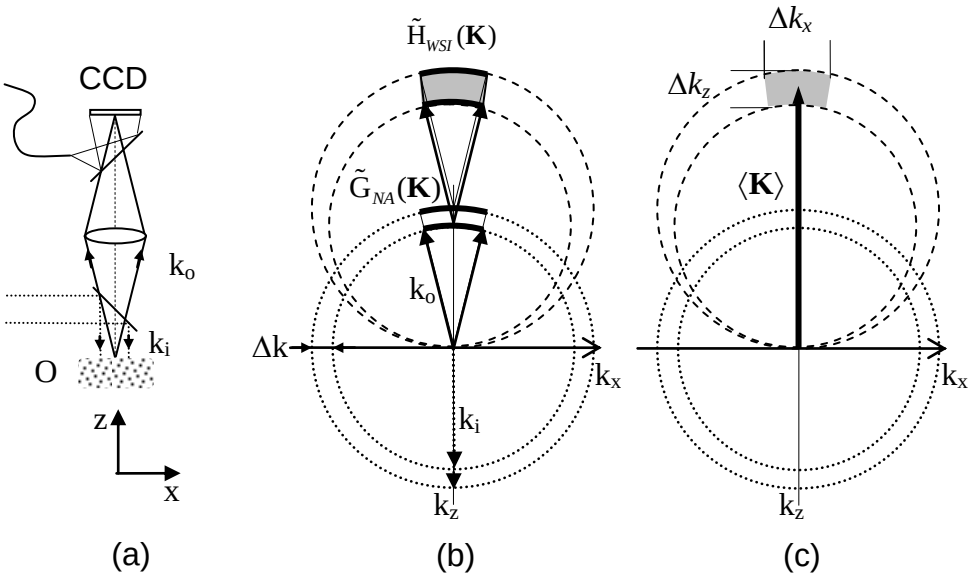

Fig. 7

Fig8
Click here to download Figure: Fig8.doc

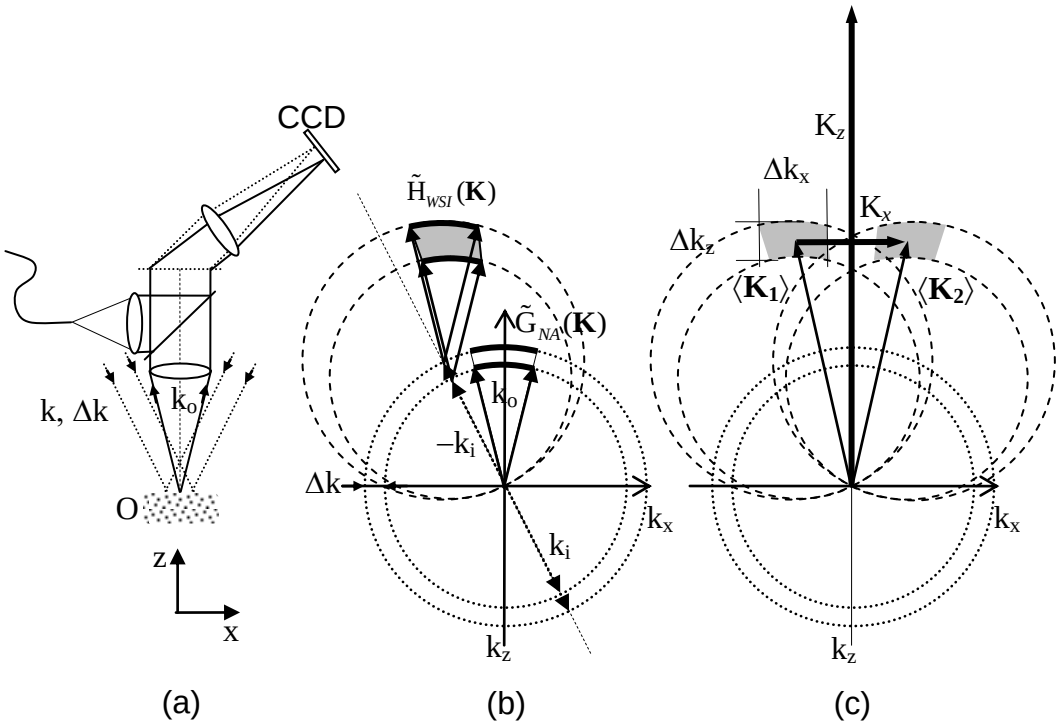

Fig. 8

Fig9a

Click here to download high resolution image

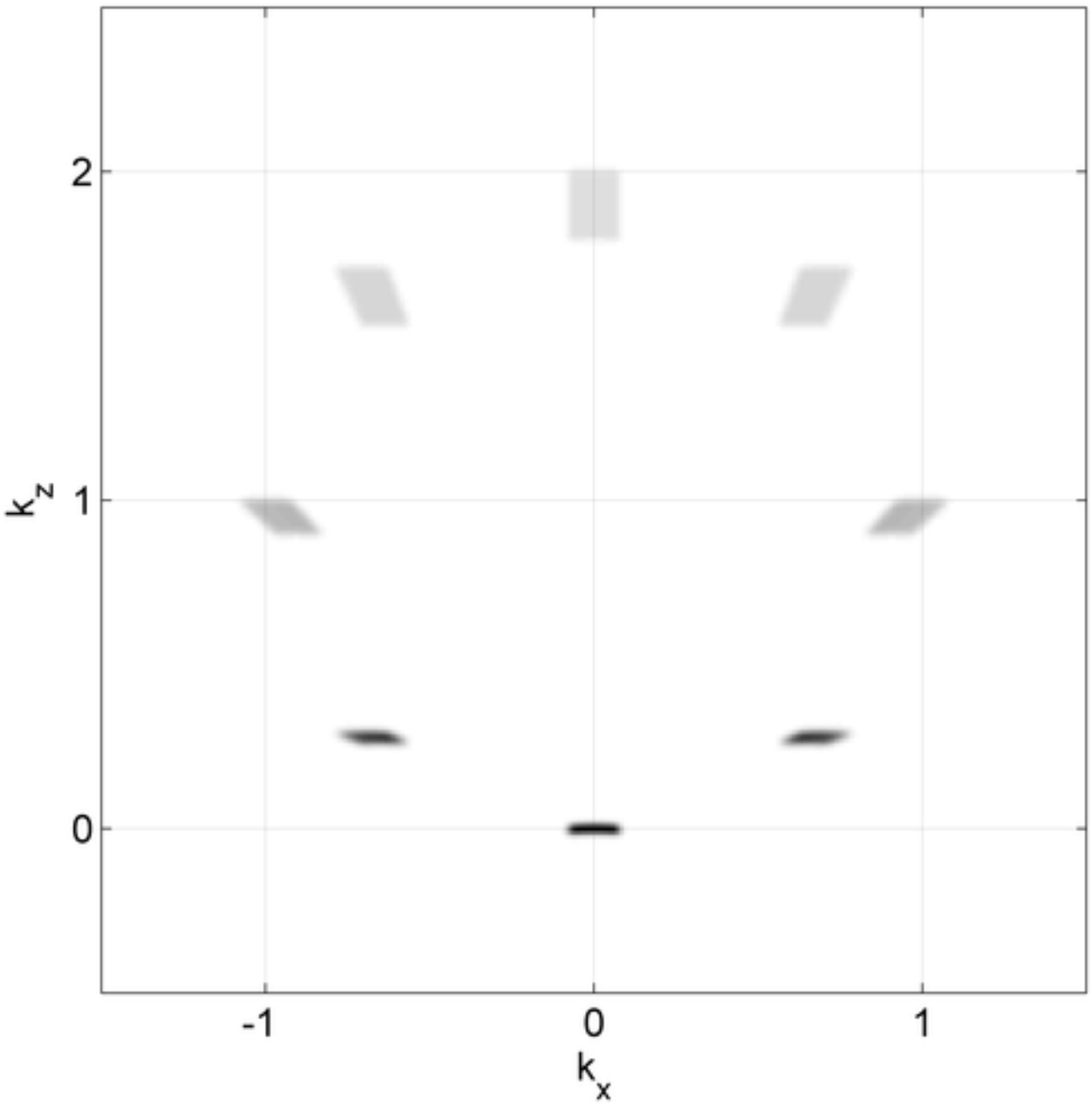

Fig9b

Click here to download high resolution image

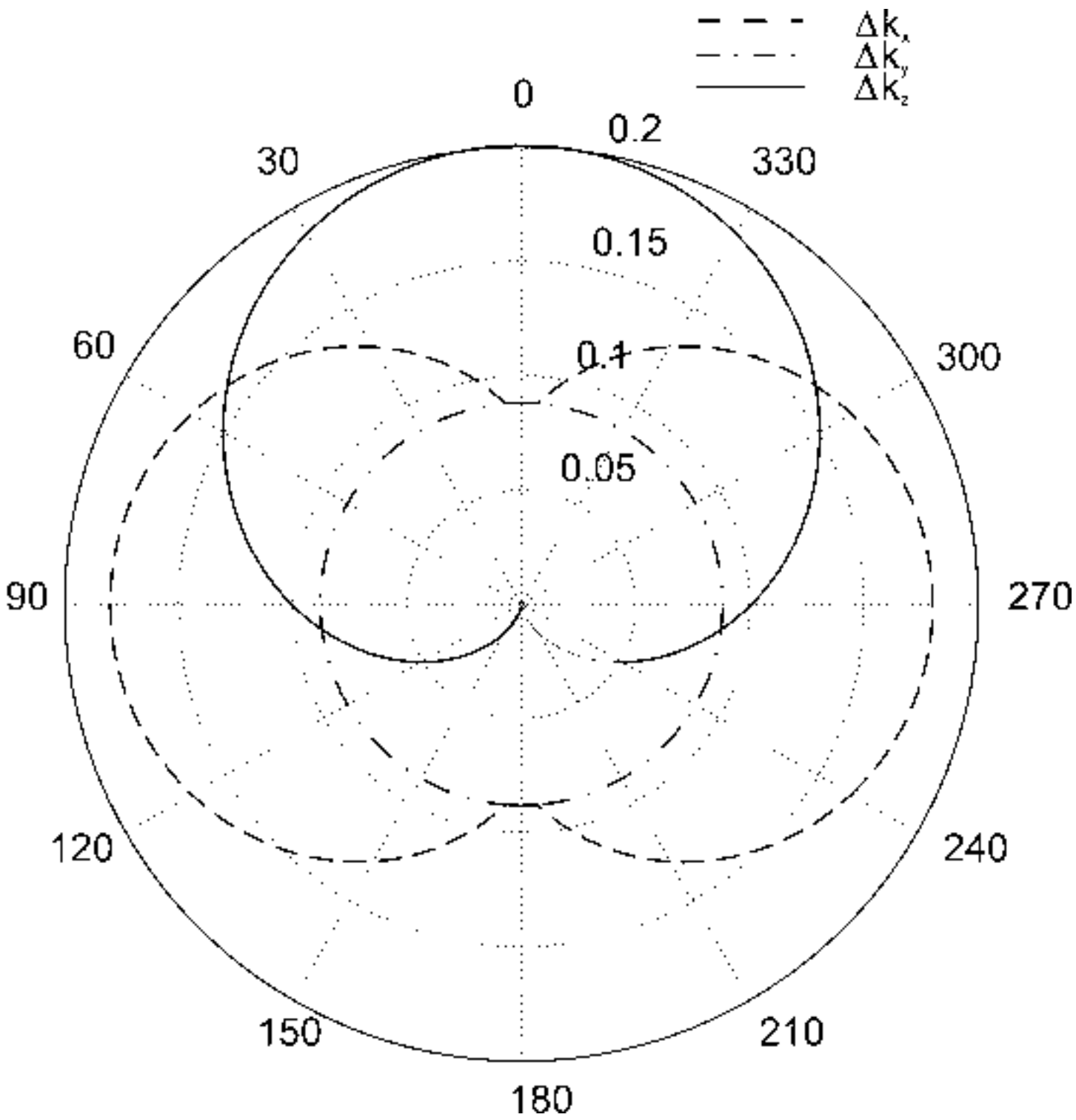

Fig10a

Click here to download high resolution image

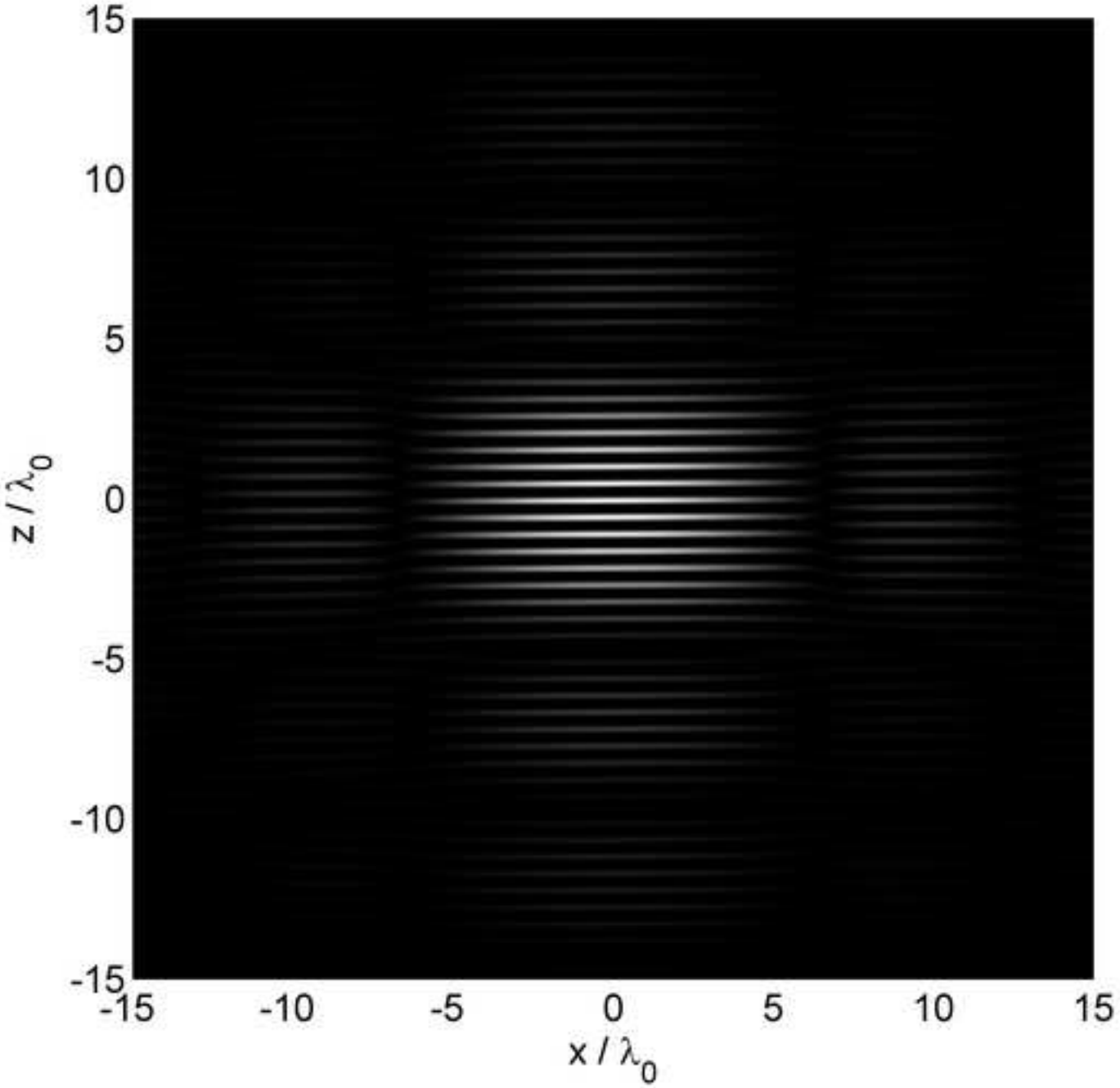

Fig10b

Click here to download high resolution image

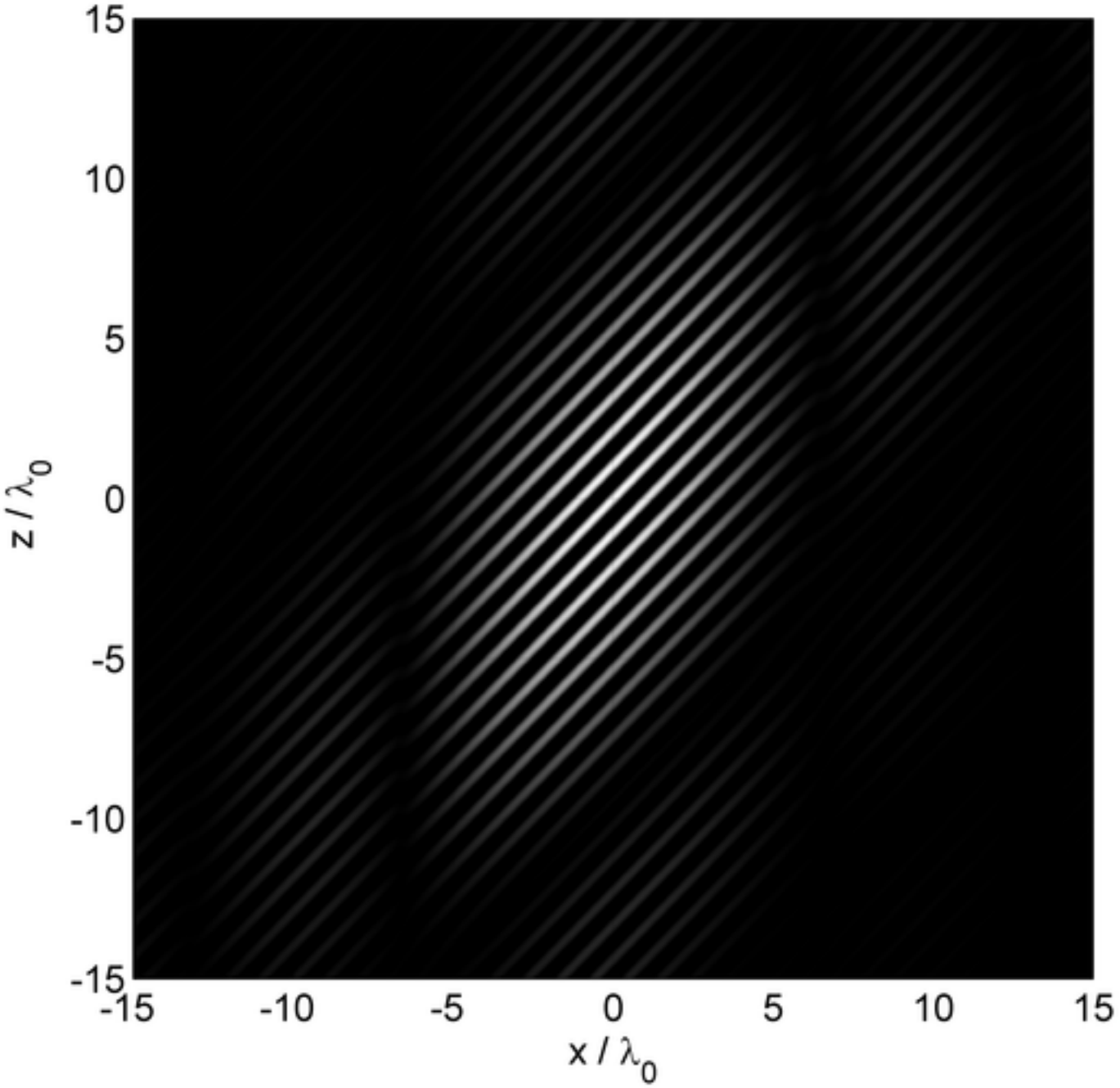

Fig10c

Click here to download high resolution image

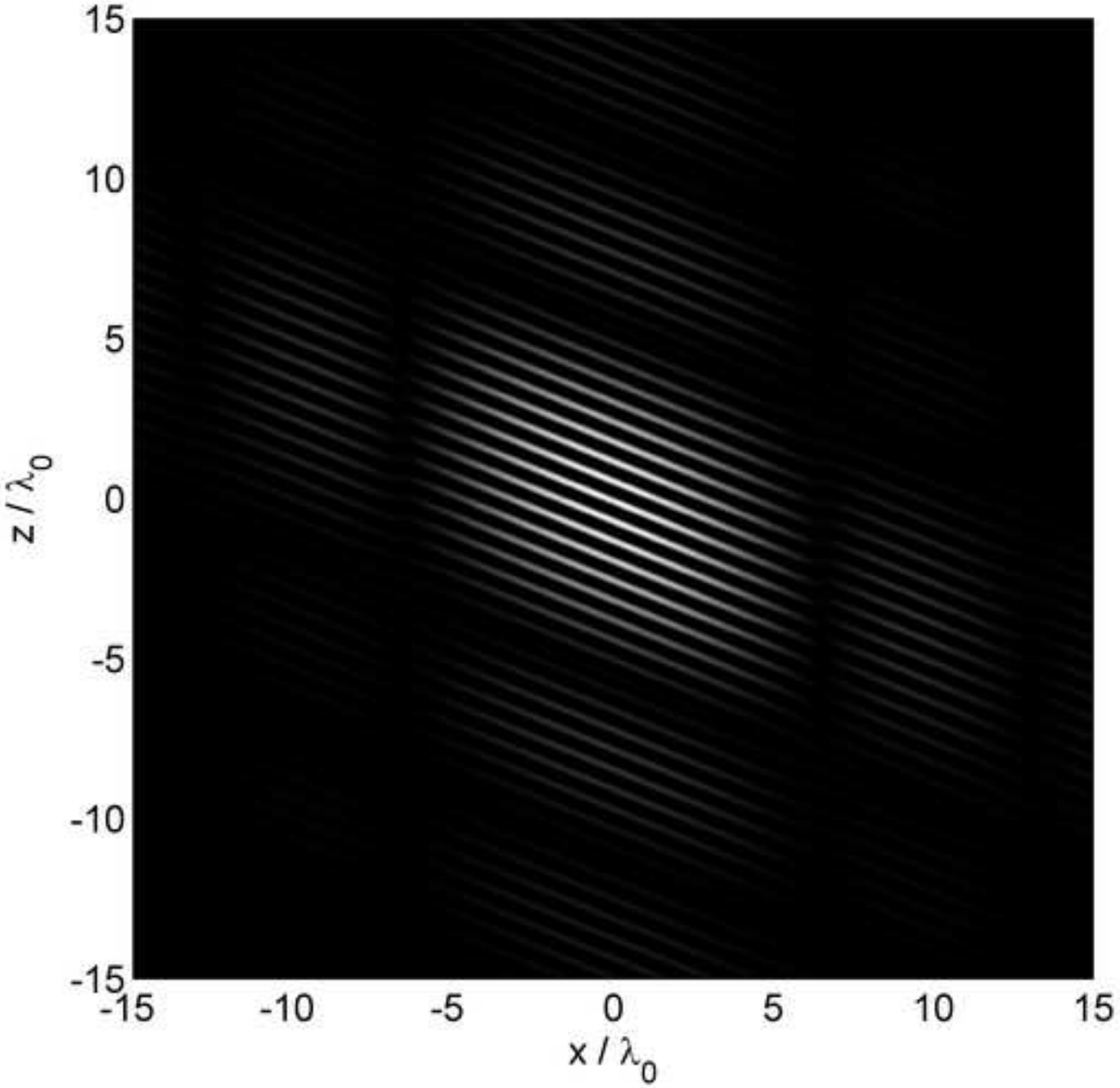

Fig10d

Click here to download high resolution image

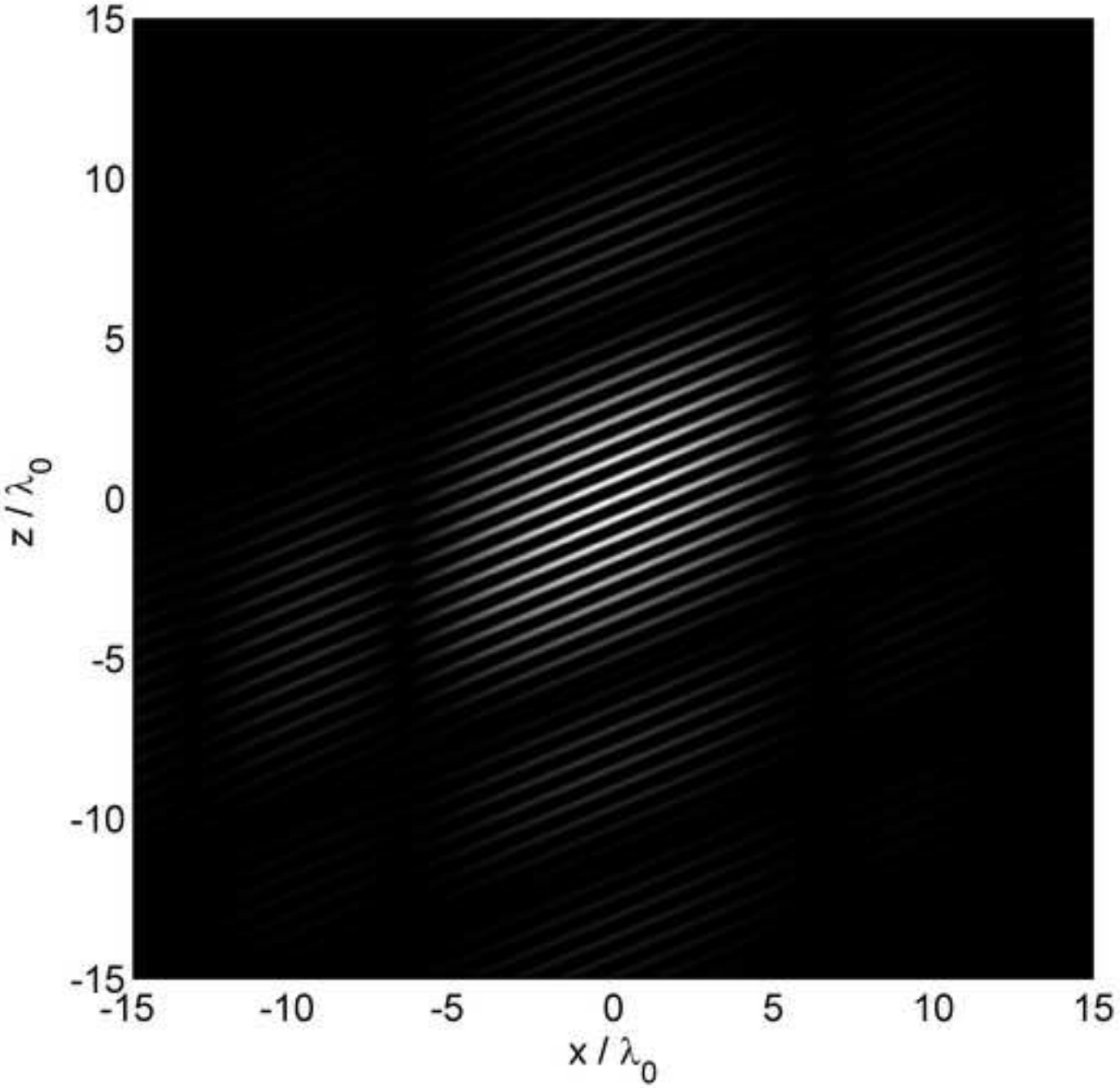

Fig11
Click here to download Figure: Fig11.doc

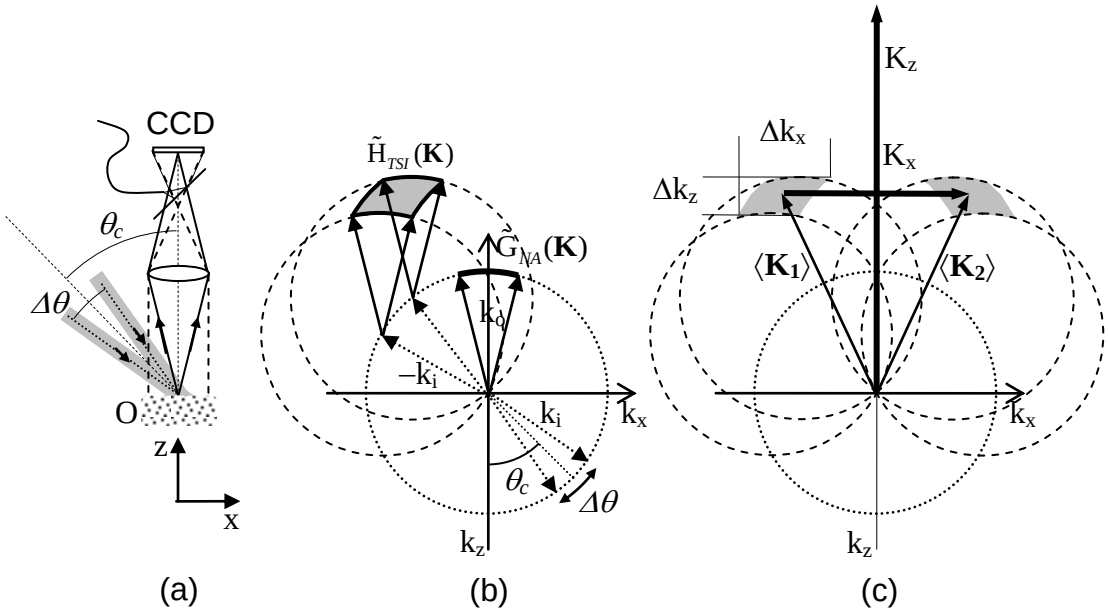

Fig. 11

Fig12a

Click here to download high resolution image

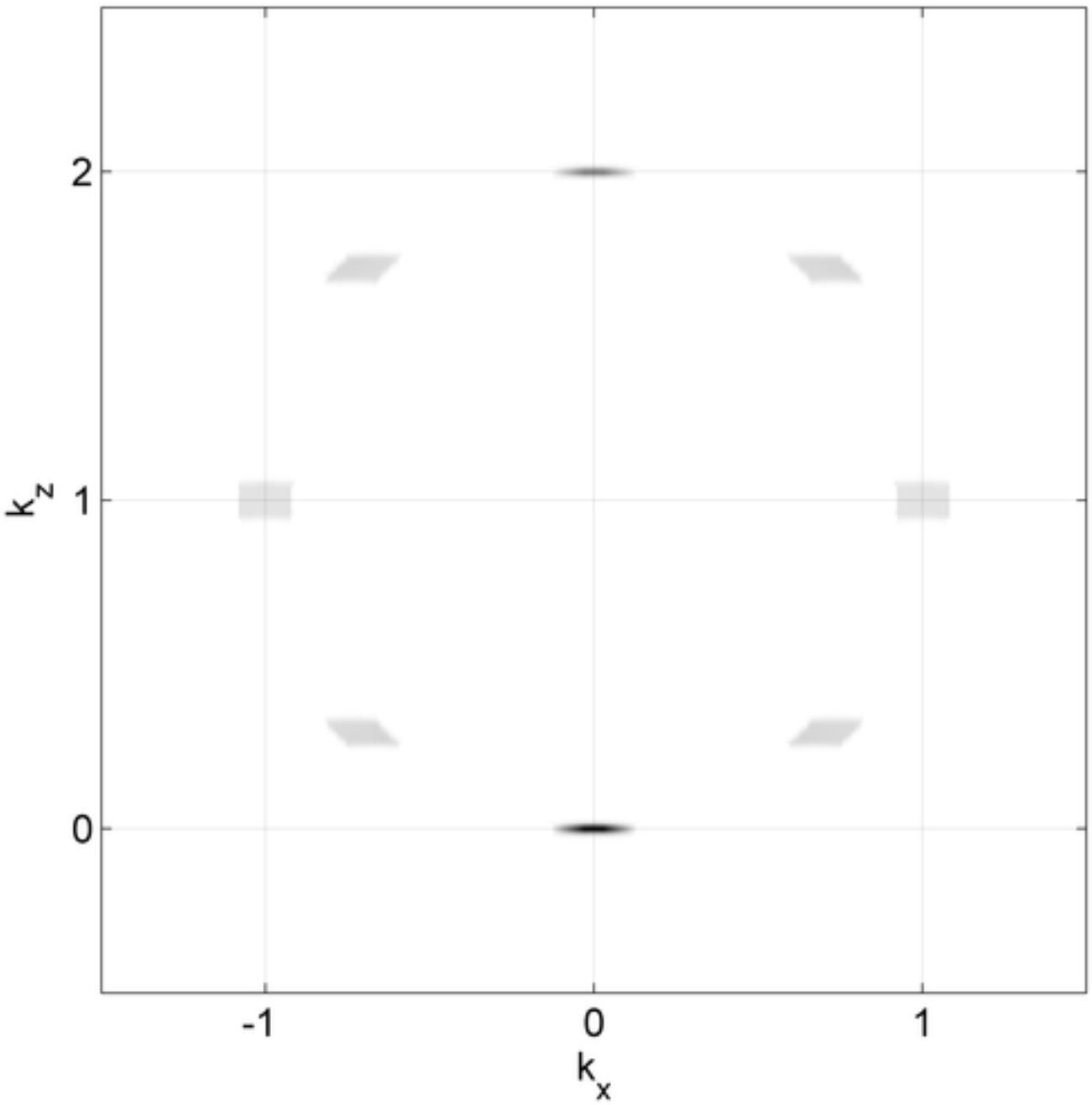

Fig12b

Click here to download high resolution image

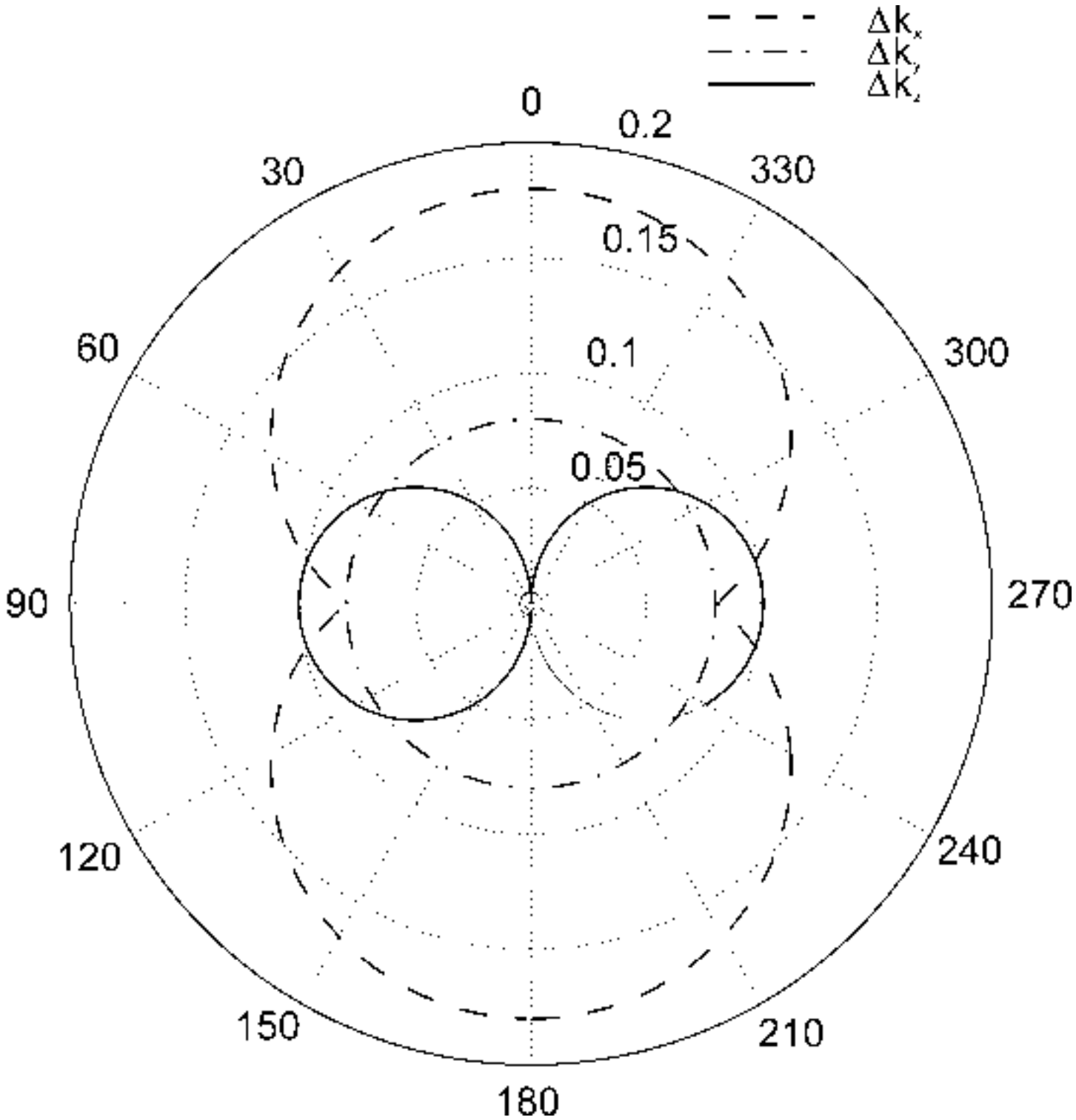

Fig13a

Click here to download high resolution image

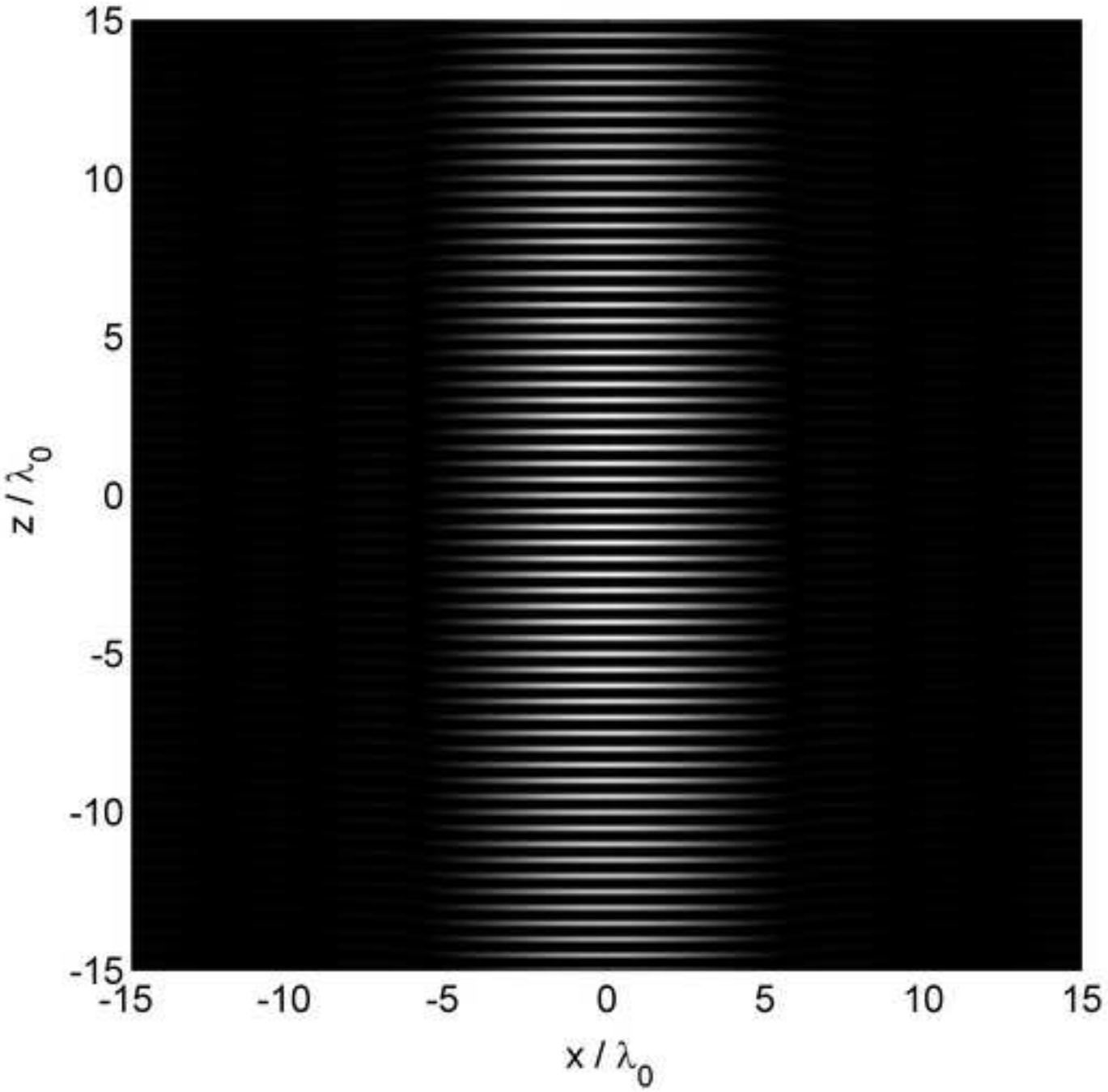

Fig13b

Click here to download high resolution image

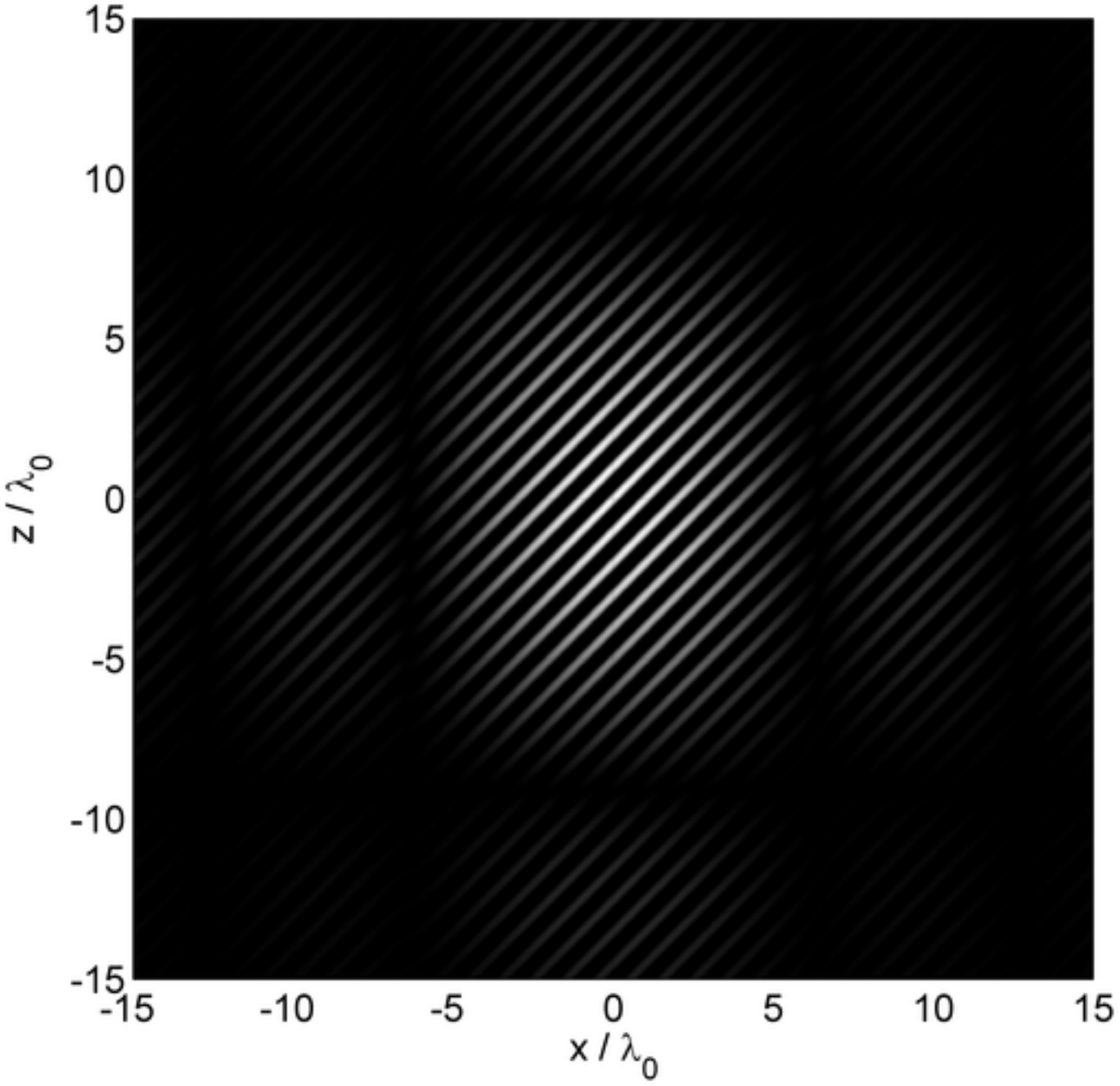

Fig13c

Click here to download high resolution image

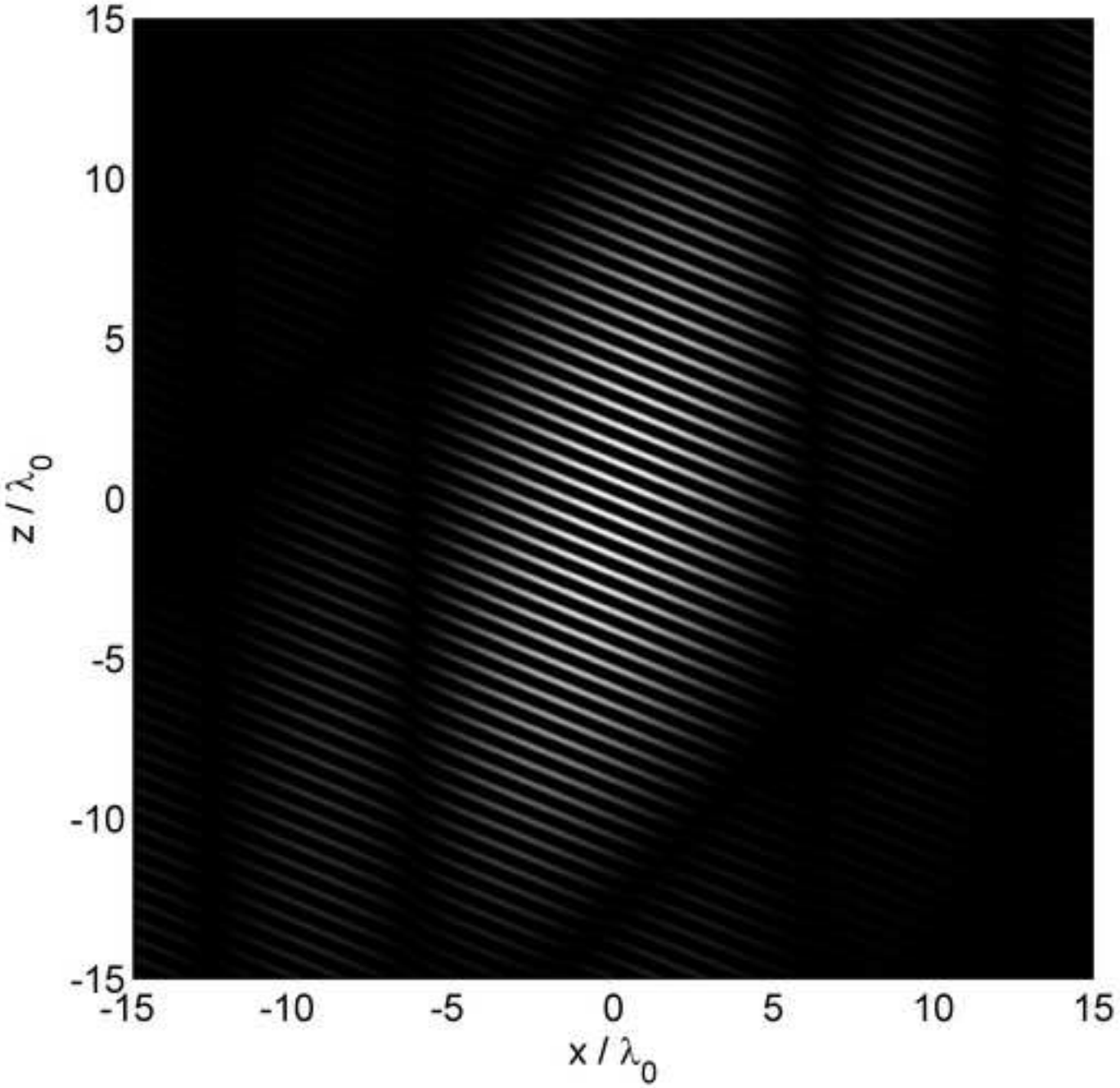

Fig13d

Click here to download high resolution image

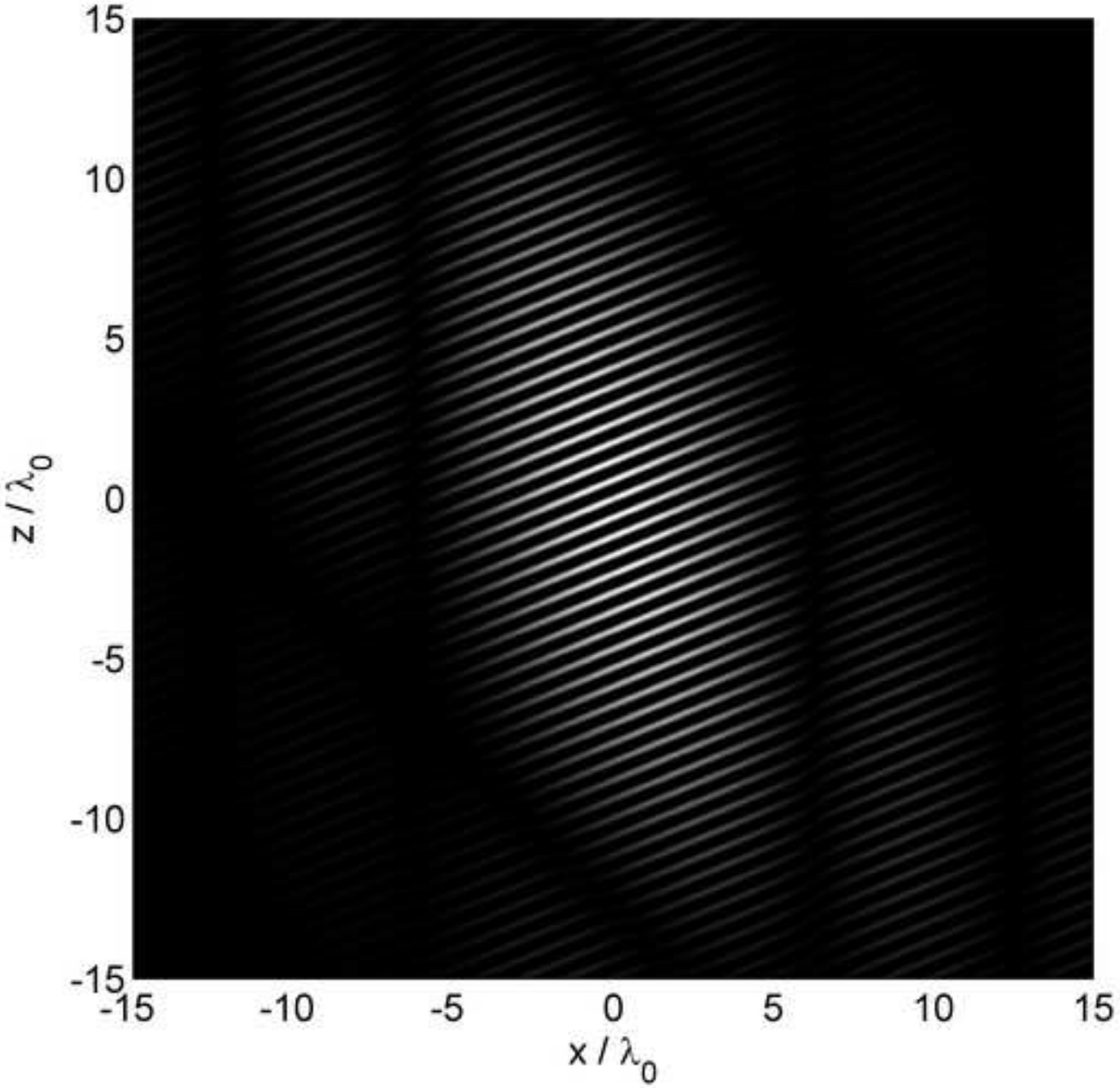

Fig14
Click here to download Figure: Fig14.doc

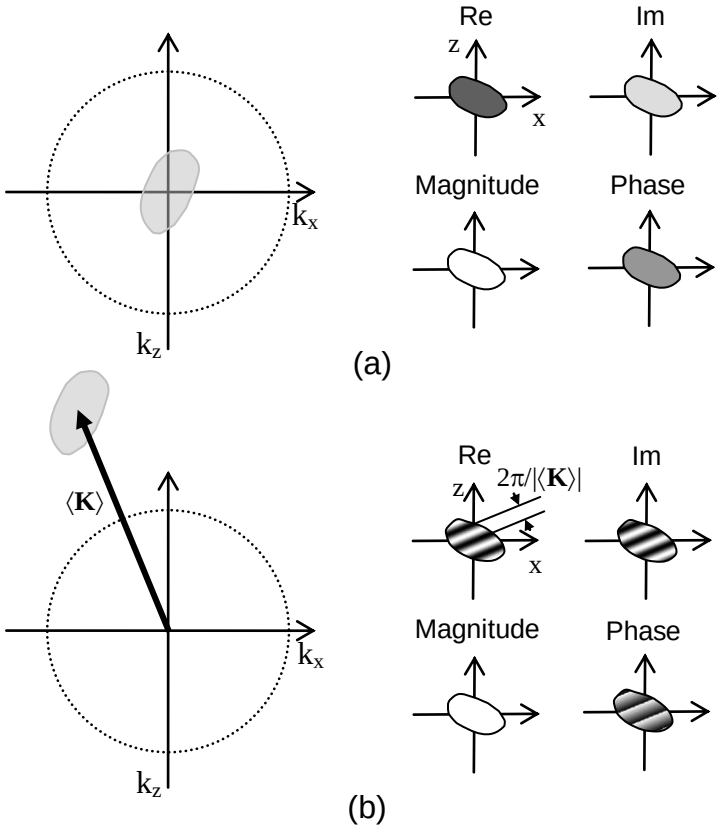

Fig. 14